CMS Analysis Note

The content of this note is intended for CMS internal use and distribution only

July 9, 2009

Prospects for the measurement of the single-top t-channel cross section in the muon channel with 200 pb^{-1} of CMS data at 10 TeV

A. Giammanco

Université Catholique de Louvain, Center for Particle Physics and Phenomenology, Louvain-la-Neuve, Belgium
Fonds National de Recherche Scientifique, Belgium

J. Bauer, J. Wagner-Kuhr, T. Müller

Institut für Experimentelle Kernphysik, Universität Karlsruhe, Germany

D. Konstantinov

Institute for High Energy Physics, Protvino, Russia

Abstract

We report on a study aiming at an early observation of single-top events produced in the t channel in proton-proton collisions, at a centre-of-mass energy of $\sqrt{s} = 10$ TeV, in the decay channel $t \to bW \to b\mu\nu$. A template-fit method is proposed, that takes advantage of the spin correlations or the invariant mass of the decay products in signal events, and the method is demonstrated to be robust against several systematic effects. This article assumes the use of 200 pb^{-1} of integrated luminosity. Under these conditions, a cross section uncertainty of $\pm 35\%$ (statistical) $\pm 14\%$ (systematic) $\pm 10\%$ (luminosity) and a sensitivity of 2.7σ are expected, assuming the standard-model prediction of $\sigma(\text{single top, t channel}) = 130$ pb.

1 Introduction

The theory of electroweak interactions predicts three different production mechanisms for single top quarks in hadron-hadron collisions [1, 2, 3], supplementary to the more abundant pair production due to the strong interaction. They are classified by the virtuality of the involved W boson: s-channel production ($q^2_W > 0$, Fig. 1(a)), W-associated, or tW, production ($q^2_W = M^2_W$, Fig. 1(b)) and t-channel production ($q^2_W < 0$, Fig. 1(c)). Recently the D0 and CDF experiments at the Tevatron $p\bar{p}$ collider both provided a 5σ observation of the electroweak mode of production [4, 5]. At the Large Hadron Collider (LHC) the reobservation is expected to happen first in the t-channel mode, by far the most abundant of the three at the energies soon to be available at the new machine, and the one with the most striking final state topology. This note treats this production mode as signal, including the other two in the definition of background.

The study of single top quark production provides a unique possibility to investigate many aspects of top-quark physics that cannot be easily studied in $t\bar{t}$ production. All the three channels are directly related to the modulus squared of the CKM matrix element V_{tb}, allowing for a direct measurement of this quantity and thus for a further test of the Standard Model, and in particular of the assumption that only three quark families exist [6, 7]. One can investigate the tWb vertex structure and FCNC couplings in the production processes, and the single-top topologies are also a window for searches for anomalous couplings and s-channel resonances like W' bosons. A review of many opportunities to observe new physics from deviations in the expected cross sections of the t- and s-channel modes can be found, e.g., in Ref. [8].

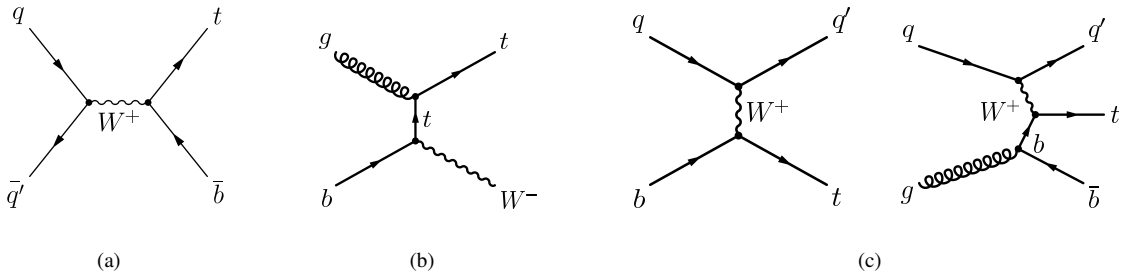

Figure 1: Leading order Feynman diagrams for single top quark production in s-channel (a), W-associated or "tW" (b), and t-channel production (c), the latter is shown in the LO description together with the dominating NLO diagram.

The goal of this note is to update and improve the analysis with respect to the study of Ref. [9], in a different scenario which anticipates the expected conditions for the very early single-top analyses: a centre-of-mass energy of 10 TeV, and an accumulated statistics of 200 pb^{-1}; these numbers correspond to the plans agreed during the Chamonix Workshop in February 2009 [10]. We also benefit from a more realistic simulation, tuned on the cosmic data acquired during the 2008 commissioning campaigns [11], and from improved reconstruction tools.

This study is based on the muonic decay channel, in which the W boson from the top quark decays further into a muon and a neutrino.

This paper is organized as follows: Sec. 2 describes the Monte Carlo samples and the software framework used; Sec. 3 discusses the event selection; Sec. 4 presents a data-driven technique for estimating the QCD background; Sec. 5 discusses the reconstruction of top quarks in the selected sample and shows how to extract the reconstructed mass and the polarization of the top quark; Sec. 6 presents the cross section extraction based on template fits to the most striking features of the signal; Sec. 7 explains in details how the systematic uncertainties have been estimated; Section 8 draws the conclusions and presents the plans for future analyses.

2 Data samples and software framework

The t-channel events from Monte Carlo simulation used in this study have been generated with the MadGraph event generator [12]. In order to give a fair approximation of the full next-to-leading order (NLO) properties of the signal, the 2→3 diagram (Figure 1(c), right-hand side), corresponding to the dominant NLO contribution to the t channel, is combined with the leading order (LO) 2→2 process (Figure 1(c), left-hand side) by a special matching procedure based on Ref. [13], giving a merged sample that describes the entire phase space while avoiding double counting. The separately generated sub-samples for the 2→2 and 2→3 processes are matched in such a way to

give a smooth $p_T^{2nd\ b}$ spectrum. The optimal matching threshold is determined under the assumption that the soft transverse momentum region of the additional b quark is best described by the 2→2 process, whereas the modeling of the high-p_T tail of the spectrum by the 2→3 process. More details on the normalization of the spectrum as well as a comparison of the outcome to other generators, including MC@NLO [14], can be found in Ref. [15]. This comparison resulted in general in a good agreement between the different generators in the kinematic region of interested for our analysis. The technical implementation of the matching inside the CMS software is realised on top of the `MadGraphInterface` package.

Several standard model processes are taken into account as background to the analysis. Table 1 summarizes the Monte-Carlo data samples for signal and backgrounds, and provides the number of events and cross section for each sample. For the signal sample generated by MadGraph, the theoretical cross section is calculated at NLO, assuming $m_{top} = 172.4$ GeV, QCD scale equal to $m_{top}/2$, and PDF set CTEQ6M [18], yielding 130.1 pb [16, 17]; this is multiplied by a leptonic branching ratio of 0.324 [19]. All the other cross sections have been taken from the references listed in Table 1 or, when no reference is given, from the generator itself.

There is a certain degree of double counting between the $W/Z + jets$ and the $W/Z + Q\bar{Q}$ samples, which is solved by using the tool described in Ref. [20], based on the so called "MLM prescription" [21]: we split and re-merge the events into the categories listed in the bottom part of Table 1.

The simulation of the full detector response is based on GEANT 4 [22], and assumes perfect alignment and calibration ("ideal scenario" in the jargon).

No pile-up was included in these samples. This is justified for this note by the expectation that the first ≈100 pb^{-1} of data will be recorded with a very low instantaneous luminosity in the range $10^{29} - 10^{31}\ cm^{-2}s^{-1}$. See Ref. [23] for the luminosity expectations during early LHC running.

The study presented in this note is performed within the CMS software release 2_2_6 and the tags listed in Table 2. The reconstructed data samples are further processed using the so called layers 0 and 1 of the Physics Analysis Toolkit (PAT) [28]. The PAT is a high-level analysis framework providing common software tools. The layer 0 performs "cleaning" tasks like isolation and duplicate removal of the standard reconstructed objects, and computes related information (e.g., lepton isolation). The output of this layer is a consistent set of AOD objects and associated information. Layer 1 then collapses the output into compact objects. Jet corrections, b tagging, Monte Carlo matching and other high-level tasks are also applied at this level. Making use of these PAT objects, we apply a pre-selection and save the surviving events in a customized ROOT "tree". The final selection is then applied in a second independent step. Both the pre-selection and the final selection criteria are described in the next section.

3 Event selection

This section provides a detailed description of the selection applied to the simulated data in order to suppress backgrounds and get a signal-enriched sample. The study presented here focuses on the muonic decay channel. The electronic channel will be the topic of a future study, and it will probably require more effort from the point of view of the rejection/estimation of fakes; the tauonic and the all-hadronic channels have probably no chance to emerge from the QCD background. The final state topology in the t channel is then characterised by exactly one isolated muon and a b jet from the top quark decay, as well as a light flavour jet produced in the forward region.

In the following we present the definition of the selected reconstructed muons, the requirements on the jets, and the tagging method used to identify b jets. In order to reject and control the QCD events able to survive the selection chain up to this point, we make use of an additional requirement on the transverse W boson mass: events above the threshold pass the selection, while those below the threshold are used in Sec. 4 to estimate the QCD contamination in the signal region. The outcome of the presented selection is scaled to the expectation corresponding to an analysed data amount of 200 pb^{-1}.

3.1 Trigger selection

All events must pass the selection of the High Level Trigger path `HLT_Mu15`, contained in the start-up trigger menu proposed for runs at an instantaneous luminosity of order $10^{31}\ cm^{-2}s^{-1}$ [29]. It requires a reconstructed muon with $p_T > 15$ GeV, within $|\eta| < 2.1$. This trigger path is expected not to need prescaling in the foreseen luminosity range.

Process	σ[pb]	Tot. events	Generator	Dataset name
single top, t channel ($W \to l\nu, l = e, \mu, \tau$)	42.9 (NLO)	281,756	MadGraph	/SingleTop_tChannel/Summer08_IDEAL_V9_v1/
single top, s channel ($W \to l\nu, l = e, \mu, \tau$)	1.6 (NLO, scaled) [24]	11,999	MadGraph	/SingleTop_sChannel/Summer08_IDEAL_V9_v1/
single top, tW channel (inclusive)	29 (NLO, scaled) [25]	169,048	MadGraph	/SingleTop_tWChannel/Summer08_IDEAL_V9_v1/
$t\bar{t}$	414 (NLO+NLL) [26]	905,369	MadGraph	/TTJets-madgraph/Fall08_IDEAL_V11_redigi_v10/
$W(\to l\nu) + jets$	(†)	(†)	MadGraph	/WJets-madgraph/Fall08_IDEAL_V9_v1
$Z/\gamma^*(\to l^+l^-) + jets$ (*)	(†)	(†)	MadGraph	/ZJets-madgraph/Summer08_IDEAL_V11_redigi_v1
$V(\to l\nu, l^+l^-) + Q\bar{Q}$ (**)	(†)	(†)	MadGraph	/VQQ-madgraph/Fall08_IDEAL_V9_v1
WW	74 (LO) [27]	204,722	PYTHIA	/WW/Summer08_IDEAL_V11_redigi_v1/
WZ	32 (LO) [27]	238,332	PYTHIA	/WZ_incl/Summer08_IDEAL_V11_redigi_v1/
ZZ	10.5 (LO) [27]	199,810	PYTHIA	/ZZ/Summer08_IDEAL_V11_redigi_v1/
μ-enriched QCD (***)	121,675 (LO)	6,300,505	PYTHIA	/InclusiveMuPt15/Summer08_IDEAL_V11_redigi_v1/

(*) $m_{ll} > 50$ GeV
(**) $V = W, Z$; $Q = b, c$
(***) $\hat{p}_T > 20$ GeV, $p_T^{\mu} > 15$ GeV
(†) separated into sub-processes:

Process	$\sigma[pb]$	Tot. events
$W+$ light partons	40,000 (LO)	9,549,245
$Wb\bar{b}$	54.2 (LO)	156,945
$Wc\bar{c}$	118.8 (LO)	529,001
Wc	1,490 (LO)	3,011,523
$Z+$ light partons	3,700 (LO)	1,205,599
$Zb\bar{b}$	44.4 (LO)	155,411
$Zc\bar{c}$	71.7 (LO)	359,235

Table 1: Datasets used in this analysis. The samples are generated either inclusively or with a final state restricted to the leptonic mode, including electrons, muons, and taus.

Tag	Package
V01-08-02	CondFormats/JetMETObjects
V05-13-02	DataFormats/HepMCCandidate
V03-18-07	DataFormats/PatCandidates
V09-30-03	PhysicsTools/HepMCCandAlgos
V04-14-24	PhysicsTools/PatAlgos
V03-05-02	PhysicsTools/PatUtils

Table 2: Tags used on top of CMSSW_2_2_6.

3.2 Object definition

Leptons

Reconstructed muons with a transverse momentum $p_{T,\mu} > 20$ GeV/c within the trigger acceptance range ($|\eta| < 2.1$) are selected. The quality of the candidate has to meet the requirements of a "global tight prompt muon", whose definition can be found in [30].

We select an exclusive muon final state and remove other leptons (electrons, muons) as described in Sec. 3.3. Electron candidates are defined, in CMS, by a basic set of requirements in ECAL and in the Tracker [31]. These criteria are quite loose and serve as the starting point of an additional classification, where three different electron categories are distinguished: loose, medium and tight; a detailed description can be found in Ref. [32]. For the purpose of top-quark analyses the tight electron category has shown to give the best fake electron rejection at a reasonable cost in efficiency [33]. Therefore, in this analysis only electron candidates of the tight ID category, with $p_{T,e} > 20$ GeV/c and $|\eta| < 2.4$, enter the lepton count.

Jets

Jets are reconstructed using the iterative cone algorithm [34] with a cone size of 0.5. The jet energy is scaled by a factor that describes the detector response depending on the transverse energy and the pseudo-rapidity of the jet [35]. In this analysis we consider only jets whose calibrated transverse momentum is larger than 30 GeV/c, within $|\eta| < 5$.

b tagging

Several b tagging algorithms are available in CMSSW. Some exploit the long B-hadrons lifetime, others their semi-leptonic decay modes and others use kinematic variables related to the high B-meson mass and hard b-quark fragmentation function. Details are provided elsewhere [36].

For this study we use the "track counting" algorithm, both in the "high purity" and "high efficiency" versions. This algorithm calculates the signed 3D impact parameter significance (IP/σ_{IP}) of all the tracks associated to the jet that pass tight quality criteria, orders them by decreasing values of this observable, and outputs as jet discriminator the value of IP/σ_{IP} for the second ("high efficiency") or third ("high purity") track. The b-tagging physics object group (POG) proposes a set of three reference thresholds (tight, medium and loose working points) for each algorithm [36], and for the track-counting family the tight working point corresponds to choose the high-purity algorithm with threshold set to 5.36, while the loose working point requires a threshold of 1.47 on the high-efficiency tagger. The advantage of sticking to these reference points lies mostly in the fact that the expected uncertainties on efficiencies and mistag rates from data-driven techniques have been evaluated in different integrated luminosity scenarios [37, 38].

In events with one identified muon and two jets, using the tight (loose) working point, we observe an efficiency of 34.0% (82.6%) for jets matched to b quarks within $\Delta R < 0.3$, with $p_T > 30$ GeV and within the Tracker acceptance ($|\eta| < 2.5$).

3.3 Lepton counting

We require the presence of exactly one muon. In order to reduce the contribution of dilepton events, which can come from $t\bar{t}$, we veto events with more than 1 lepton, where also electrons are considered in the count.

3.4 Near-jet veto

If the reconstructed muon is closer than $\Delta R = 0.3$ to one of the identified jets, the event is rejected.

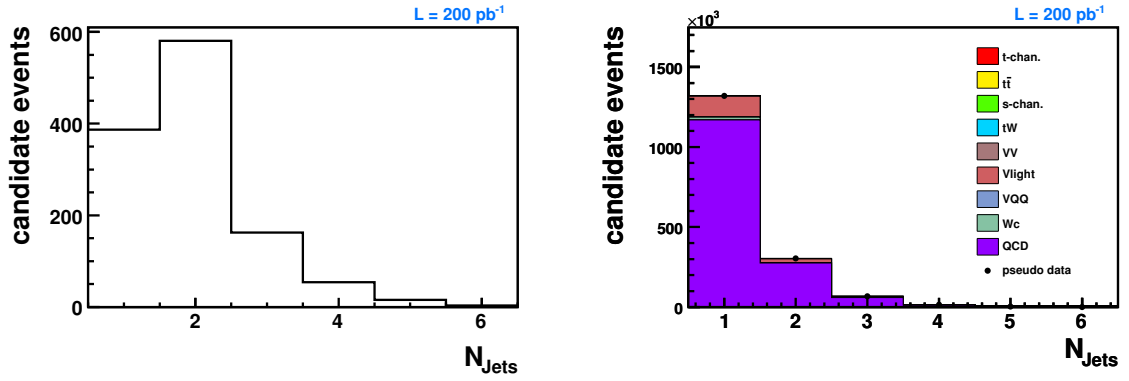

(a) (b)

Figure 2: Jet multiplicity after the lepton counting and the near-jet veto; only events with at least one jet are shown. Signal only (a) and all processes (b), scaled to 200 pb^{-1}. Here, and in the following figures, $V = W/Z$, $Q = c/b$, and "light" is short-hand for light partons.

3.5 Jet counting

Figure 2(a) shows that in most of the signal events two jets are reconstructed with the conditions outlined in Sec. 3.2, therefore the present study focuses on the 2-jets sub-sample. Figure 2(b) shows that at this stage of selection (i.e., after lepton counting and near-jet veto) the sample is still dominated by processes without b quarks. This problem is specifically addressed in Sec. 3.7.

3.6 Muon isolation

Although the definition of the muon object contains quality requirements, and despite the near-jet veto, a considerable amount of QCD events remains due to the selection of muons from B hadron decays or decays in flight. Their contribution can be significantly suppressed by a cut on the isolation of the reconstructed muon object. We define the combined relative isolation as

$$relIso = \frac{p_{T,\mu}}{p_{T,\mu} + tkIso + caloIso} \,, \tag{1}$$

where $tkIso$ ($caloIso$) is the sum of the transverse momenta (transverse energies) of the tracks (calorimeter deposits) in a cone of size $\Delta R < 0.3$ around the muon direction, excluding the track (calorimetric footprint) of the muon itself. More details can be found in Ref. [39].

This variable is shown in Fig. 3 for the selected muon in the 2 jets sample. In contrast to the processes where the muon comes from the decay of a W, the QCD contribution does not accumulate at 1. Therefore, the QCD rejection can effectively be improved by requiring the relative isolation of the reconstructed muon to be above 0.95.

3.7 b counting

The signature of the t-channel single-top production includes 3 partons in the final state, see Fig. 1(c): one light quark recoiling against the virtual W boson, one b quark from the top-quark decay, and a second b quark from the initial gluon splitting. Since the second b quark is most likely produced at very high rapidities, i.e., outside the tracker acceptance of $|\eta| < 2.5$ and thus not allowing b tagging to be performed, we expect most signal events to have only one b-tagged jet. The highest discriminator value of the high-purity track-counting b tagger in the event is shown in Fig. 4(a), and the b-tag multiplicity in 2-jets events is shown in Fig. 4(b). The contribution of processes without b quarks in the final state is strongly suppressed in the 1-tag sub-sample, showing the largest population of signal events at the same time; the small 2-tags sub-sample is dominated by $t\bar{t}$. Therefore, selected events are required to have exactly one b-tagged jet.

This requirement is further tightened by rejecting the event if the jet which fails the tight b-tagging selection passes the loose one; we call this requirement "b veto" in the following. Figure 5 shows the high-efficiency discriminator

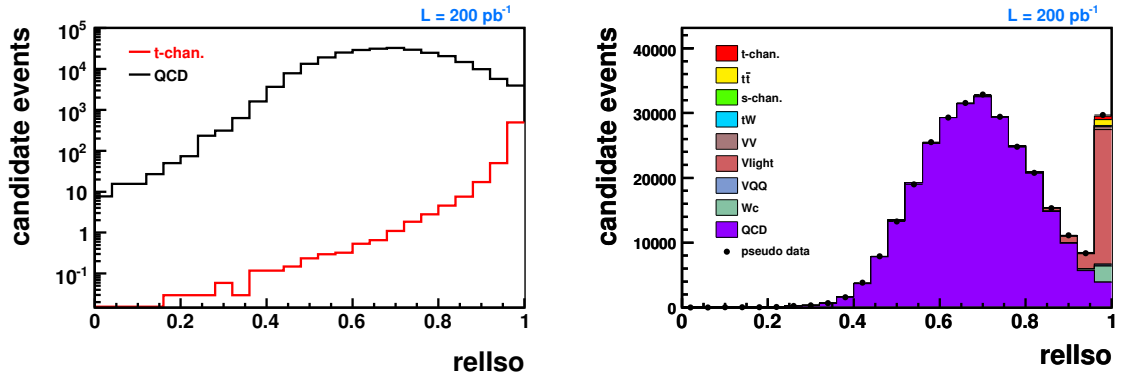

Figure 3: Relative isolation ($relIso$) of the selected muon after the requirement of exactly 2 jets, for signal and QCD (a) and all processes (b), scaled to 200 pb^{-1}.

value for the jet that fails the cut on the high-purity one; above the loose-working-point threshold (set at 1.47) the sample is dominated by $t\bar{t}$.

3.8 Transverse W boson mass

To further suppress contributions from processes where the lepton does not come from a leptonically decaying W boson, a selection based on the reconstructed transverse W-boson mass is applied. This quantity is defined as:

$$M_T = \sqrt{(p_{T,\mu} + p_{T,\nu})^2 - (p_{x,\mu} + p_{x,\nu})^2 - (p_{y,\mu} + p_{y,\nu})^2}\,, \tag{2}$$

where the transverse momentum components of the neutrino are approximated by the components of the missing transverse energy, $\vec{\not{E}}_{\mathrm{T}}$. This is corrected for the presence of muons, and the calorimetric clusters associated to jets are assigned the calibrated jet momenta [40].

Figure 6 shows the shape of the M_T distribution after the preceding selection. The QCD background can be nicely distinguished, since the transverse mass of the alleged W bosons accumulates at low values while all processes with real W bosons tend to cluster around the W mass (this feature is known in the literature as "Jacobian peak"). Hence, the reconstructed transverse W-boson mass is required to be above 50 GeV/c^2 for the event to be kept.

This variable is preferred over a simple $\not{E}_{\mathrm{T}}$ cut because of its larger separation power between signal and QCD [41], its better stability against variations of the $\not{E}_{\mathrm{T}}$ scale (see Sec. 7.2), and because $\not{E}_{\mathrm{T}}$ turns out to be quite correlated with muon momentum and muon isolation in our QCD sample, since most of the surviving QCD events have a true muon coming from b or c decay, therefore they also have a true neutrino. Moreover, differently from $\not{E}_{\mathrm{T}}$, the M_T distribution is roughly similar for all non-QCD events, and this permits a very simple way to extract the amount of QCD background from data, as presented in Sec. 4.

3.9 Summary of the selection, and results after 200 pb^{-1}

The relative impact of the presented event selection, step by step, on the signal and the considered background contributions is shown in Table 3. The expected final event yield, scaled to an integrated luminosity of 200 pb^{-1}, is shown in the last column. Among the selected signal events, 98% come from the $t \to W \to \mu$ sub-sample.

After the leptonic selection the sample is still dominated by QCD, despite the isolation requirements on the reconstructed muon. This motivates the use of the combined isolation variable $relIso$, and an additional selection on the transverse W-boson mass allows a good QCD reduction. Nevertheless, QCD remains one of the most difficult backgrounds to predict, and Sec. 4 will be entirely devoted to a data-driven method to estimate its contribution.

The second most dominating background after the leptonic selection, W+jets, is reduced significantly by the use of b tagging. Among the remaining background contamination, most events contain two b quarks in the final state (e.g., $t\bar{t}$, $Wb\bar{b}$, single top in s channel) while the presence of just one visible b quark is a specific feature of the signal (shared with tW); thus we further enhance the S/B ratio by a veto on a second b-tagged jet, with a looser threshold.

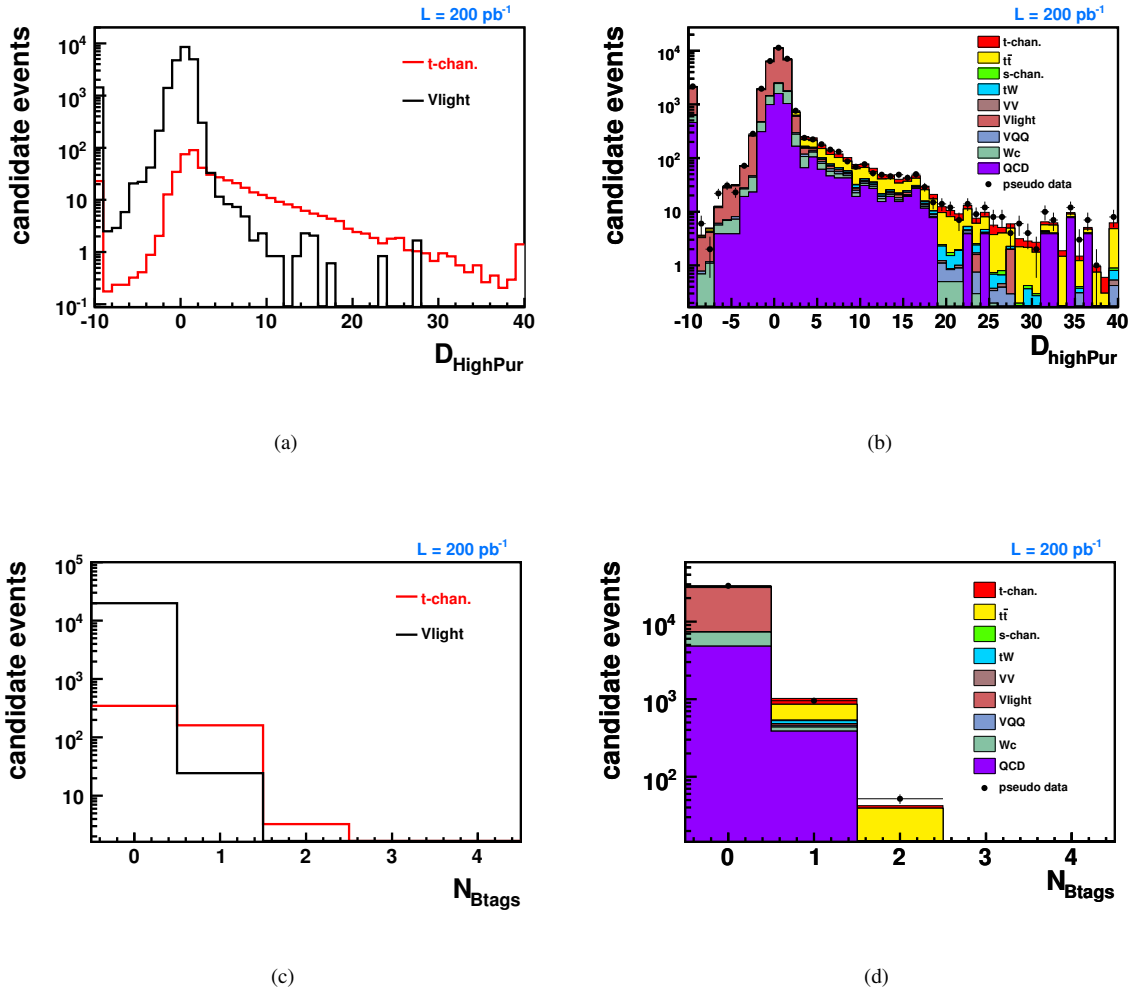

Figure 4: Highest discriminator value for the high-purity track-counting algorithm for signal and V plus light partons (a) and all processes (b), and number of tags for $D_{highPur} > 5.36$ for signal and V plus light partons (c) and all processes (d), after the 2 jets request.

It can be seen that the dominant residual background is $t\bar{t}$, despite the cuts explicitly devised against it (the dileptonic veto, the aforementioned b veto), therefore it is interesting to look at the relative importance of the different final states of this process. As shown in Table 4, the subset of $t\bar{t}$ events passing our selection is dominated by $\mu + jets$ events.

Based on the estimations for 200 pb^{-1}, we obtain $S/B = 0.45$, $S/\sqrt{B} = 6.7$ and $S/\sqrt{S+B} = 5.6$ from this selection. Due to the size of the background contamination with respect to the signal, we would need a very precise control of the backgrounds in order to find an evidence of signal through a simple event counting, in this scenario. Instead, on top of this selection, in Sec. 6 the full shapes of a couple of discriminating variables are exploited in order to extract the signal, while minimizing the need of assumptions about the main background processes.

4 QCD background estimation

Monte Carlo estimations of the QCD contamination have to be considered particularly unreliable for the purposes of our analysis, because only extreme kinematical regions pass this kind of selection, and tail effects are the most difficult to simulate properly. These arguments lead to the conclusion that only *in situ* data-driven estimations will give the needed confidence on the amount of this background.

Here we propose to extract the relative QCD and signal-like contributions from the M_T shape, after all other cuts

Process	N_{tot}^{MC}	1 iso μ	2 jets	1 tight b tag	loose b veto	$M_T > 50$ GeV	N_{sel}^{MC}	ϵ_{sel}^{tot}	N_{evt} in 200 pb^{-1}
single top, t channel	281,756	13.4%	48.2%	31.5%	82.1%	72.9%	3,441	1.22%	102±1.8
single top, s channel	11,999	11.1%	47.2%	39.4%	39.1%	68.0%	66	0.55%	1.8±0.2
single top, tW	169,048	7.9%	33.0%	28.4%	76.9%	67.6%	647	0.38%	22.3± 0.9
$t\bar{t}$	905,369	7.0%	16.6%	33.4%	59.5%	70.8%	1,485	0.16%	136.0±3.5
QCD (μ-enriched)	6,300,505	0.1%	14.9%	7.4%	86.0%	3.5%	3	0.000048%	12±6.7
Wc	3,011,523	6.3%	13.6%	1.9%	87.4%	67.2%	297	0.0099%	29±1.7
$Wb\bar{b}$	156,945	3.7%	19.9%	28.9%	49.6%	69.5%	116	0.0739%	8.0±0.7
$Wc\bar{c}$	529,001	3.3%	14.8%	2.1%	74.1%	67.5%	27	0.0051%	1.2±0.2
$W+$ light partons	9,549,245	1.8%	14.2%	0.12%	72.4%	66.7%	14	0.0001%	12±2.6
$Zb\bar{b}$	155,411	2.7%	17.2%	24.8%	71.8%	36.2%	47	0.0302%	2.7±0.4
$Zc\bar{c}$	359,235	2.9%	14.0%	2.0%	86.2%	24.0%	6	0.0017%	0.2±0.1
$Z+$ light partons	1,205,599	1.6%	14.0%	0.36%	80.0%	50.0%	4	0.0003%	2±1.2
WW	204,722	6.8%	36.7%	0.6%	80.7%	52.0%	13	0.0064%	0.9±0.3
WZ	238,332	3.8%	37.8%	4.3%	48.3%	61.1%	44	0.0185%	1.2±0.2
ZZ	199,810	1.1%	38.8%	5.9%	56.0%	60.7%	17	0.0085%	0.17±0.04
Total background									229±8.4
S/B		0.005	0.016	0.18	0.21	0.45			

Table 3: Relative selection efficiencies calculated for each selection step with respect to the preceding one. The last column shows the number of selected events rescaled to 200 pb^{-1}, with uncertainty from MC statistics.

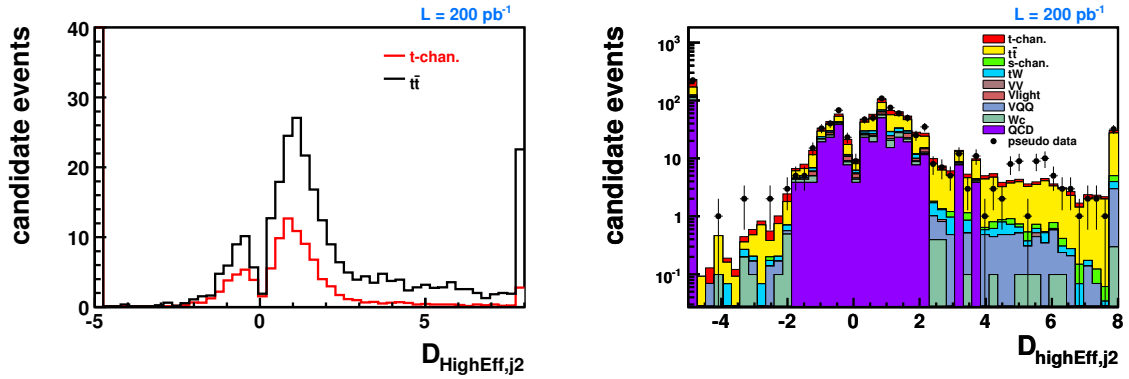

(a) (b)

Figure 5: Discriminator value for the high-efficiency track-counting algorithm for the jet that fails the cut on the high-purity one, after the 2 jets request, for signal and $t\bar{t}$ (a) and for all processes (b). The underflow bin contains jets with not enough good tracks to calculate the discriminator; this includes jets outside of the Tracker acceptance.

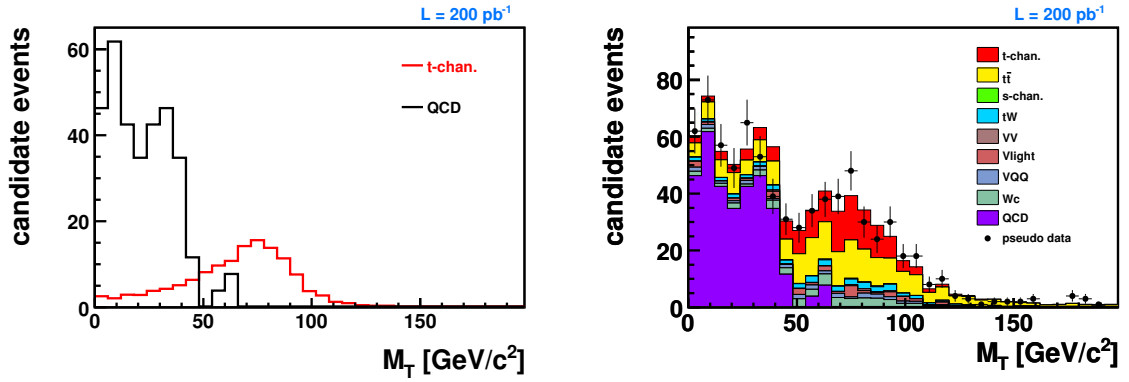

(a) (b)

Figure 6: Transverse mass after the entire selection minus the M_T cut, for signal and QCD (a) and for all processes (b).

have been applied, by parametrizing the overall distribution as

$$F(M_T) = a \cdot S(M_T) + b \cdot B(M_T)\ , \tag{3}$$

where $S(M_T)$ and $B(M_T)$ are the expected distributions for signal-like and QCD events respectively, letting only a and b fluctuate in the fit. Here and in the following, with signal-like events we mean all events where the muon comes from the decay of a W boson.

Since we wish to avoid, as much as possible, model dependent assumptions, especially for QCD, we extract $S(M_T)$ and $B(M_T)$ from control samples designed to have high statistics and to be kinematically similar to the selected sample.

Figure 7 shows that the M_T distributions for the most relevant processes are not significantly affected by b-tagging and isolation requirements. This suggests the idea of removing or inverting these two cuts in order to enlarge the statistics for control samples. In particular, in order to extract a QCD-enriched sample, we apply a dedicated selection which differs from the standard one by the absence of b-tagging requirements and by an anti-isolation cut ($relIso < 0.8$) intended to get rid of most of the signal-like events. The event yields for this selection are given

Channel	fraction
$\mu + jets$	59.1%
$\ell + \tau$	26.1%
2ℓ	12.1%
others	2.8%

Table 4: Final state composition of the $t\bar{t}$ events that pass the full selection ($\ell = e, \mu$).

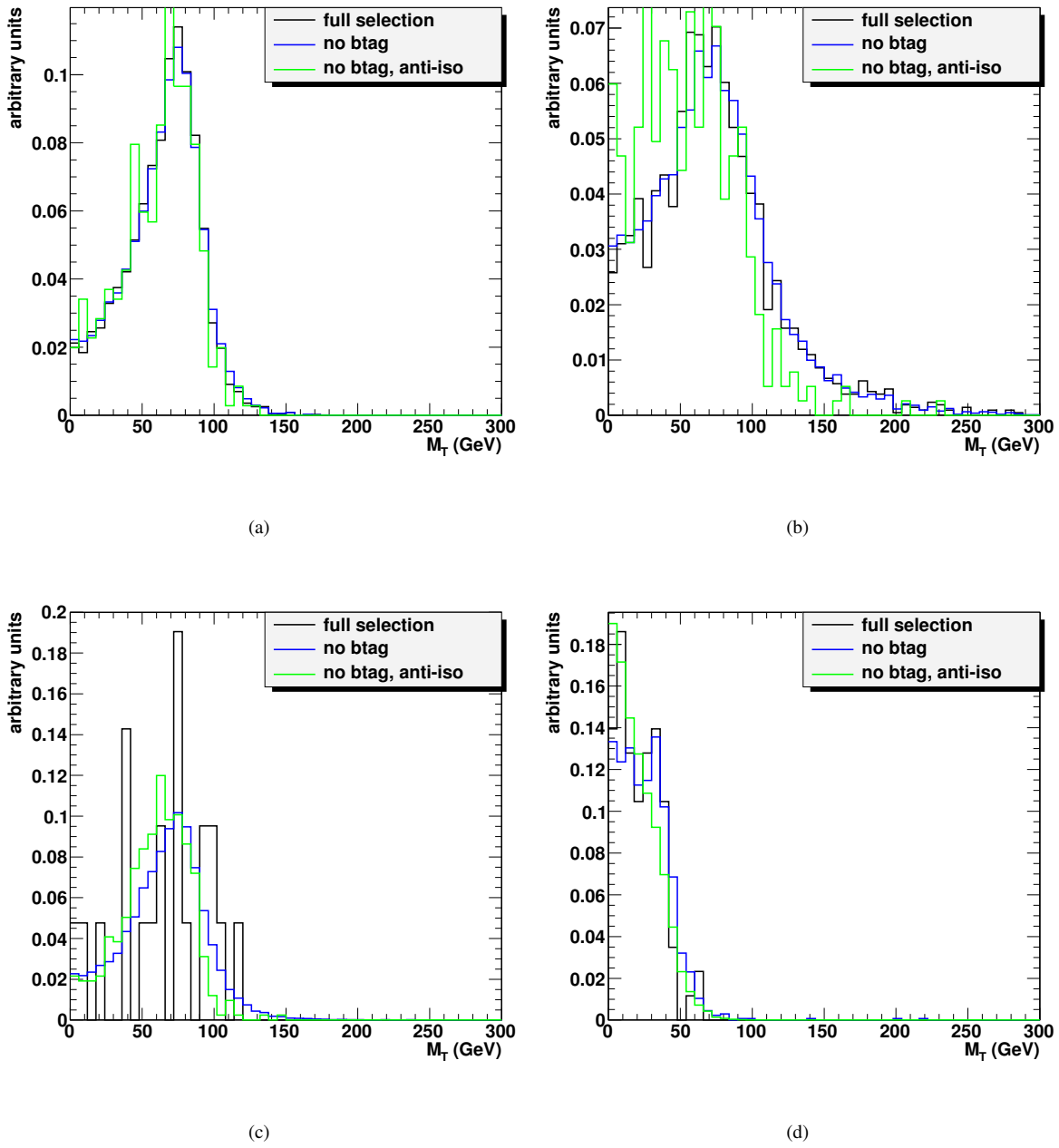

Figure 7: M_T distributions for signal (a), $\bar{tt}$ (b), $W + jets$ (c), and muon-enriched QCD (d), after the standard selection (black), a selection which differs by the removal of b tagging (blue), and by an anti-isolation cut, $relIso < 0.8$ (green).

Process	N_{evt} in MC	N_{evt} in 200 pb^{-1}
QCD	56,920	222,036
signal	352	10
$t\bar{t}$	384	30
tW	118	4
$W+$ light partons	417	340
Wc	282	28
$Wb\bar{b}$	21	1

Table 5: Event yield for the main processes in the QCD-enriched selection.

Process	N_{evt} in MC	N_{evt} in 200 pb^{-1}
QCD	1,342	5,235
signal	18,240	544
$t\bar{t}$	10,528	845
tW	4,379	150
$W+$ light partons	23,815	19,439
Wc	25,941	2,567
$Wb\bar{b}$	1,165	80

Table 6: Event yield for the main processes in the W-enriched selection.

in Table 5, and the M_T distribution shown in Fig. 9(a) is fitted to a polynomial of rank 4 in order to extract the $B(M_T)$ shape.

Figure 8 demonstrates that the M_T shape is almost the same for signal and $W + jets$ events, and still quite similar for $t\bar{t}$ despite the occasional presence of events with two final-state neutrinos which broaden the distribution. Since this QCD estimation can afford a certain degree of approximation, and since the modeling of the signal-like components turns out to be uncritical for this study, the following options have been considered for the extraction of $S(M_T)$:

- use of Monte Carlo, fitting $S(M_T)$ to a pure $W+$ light partons sample selected without b tagging, as in Fig. 8;
- use of a W-enriched control sample, which differs from the standard selection only by the absence of b tagging, see Table 6 and Fig. 9(b); it is apparent that a significant QCD contamination spoils the reliability of this sample as a signal model for low M_T;
- use of a Z-enriched control sample, obtained with a dedicated selection requiring at least two leptons, where the leading two are muons whose invariant mass is in the range $76 < M_{\mu\mu} < 106$ GeV, and two jets selected as in the standard selection apart from the absence of b tagging.

In the Z-enriched case the definition of the M_T variable is slightly different since we rescale the momenta of the two leading muons by M_W/M_Z, we treat one of them (randomly chosen) as a neutrino, and we add vectorially its transverse momentum to $\not{E}_{\rm T}$. The distribution obtained in this way has a maximum in the same position as the signal-like events with the standard M_T definition, and in general well reproduces the high-M_T region while it is significantly different in the low-M_T one, see Fig. 8. This selection yields a very pure $Z + jets$ sample, see Table 7 and Fig. 9(c).

Process	N_{evt} in MC	N_{evt} in 200 pb^{-1}
$Z + jets$	2,732	1,677
$Zc\bar{c}$	1,198	48
$Zb\bar{b}$	791	45
QCD	1	4
signal	76	2
$t\bar{t}$	530	48
$W+$ light partons	4	3

Table 7: Event yield for the main processes in the Z-enriched selection.

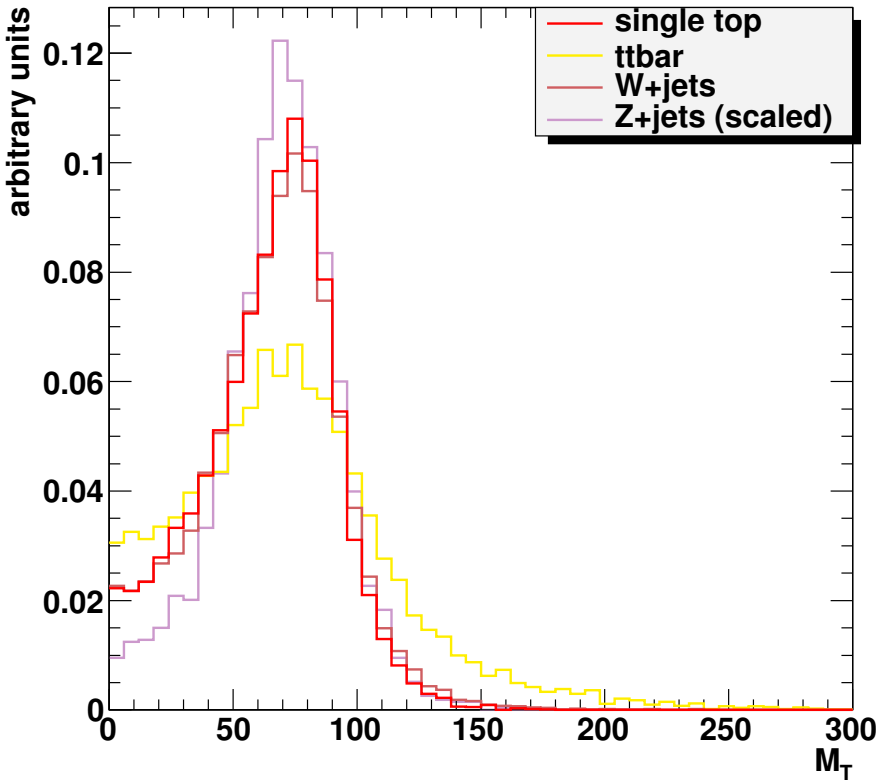

Figure 8: M_T distributions for some signal-like processes: signal (red), $t\bar{t}$ (yellow), W + light partons (brown), and Z + light partons (violet). The events from the first three categories have passed the standard selection apart from b-tagging, while the Z + light partons events have passed a dedicated di-leptonic selection and have a different definition of M_T, as explained in the text.

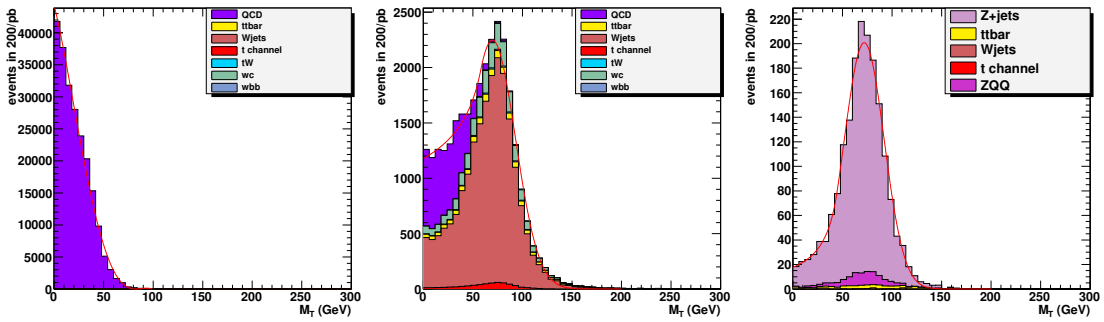

(a) (b) (c)

Figure 9: M_T distributions normalized to 200 pb^{-1} for QCD-enriched (a), W-enriched (b), and Z-enriched (c) control samples.

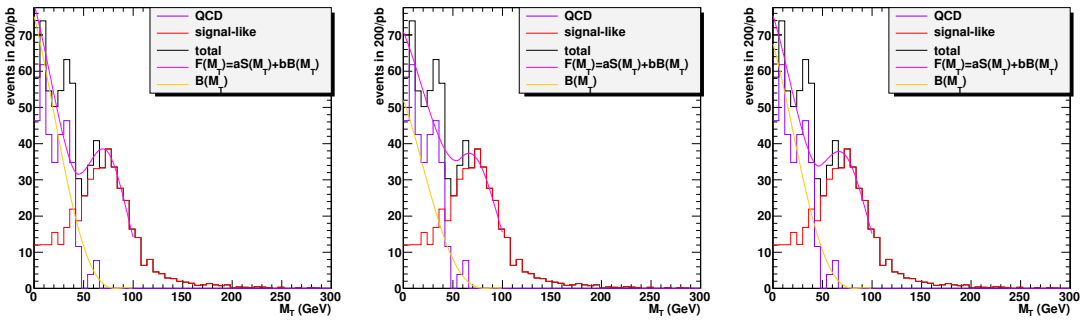

(a) (b) (c)

Figure 10: M_T distributions normalized to 200 pb^{-1} for events passing the standard selection. In the global fit to $F(M_T) = a \cdot S(M_T) + b \cdot B(M_T)$, the $B(M_T)$ function comes from the QCD-enriched sample and $S(M_T)$ from the Z-enriched sample (a), the W-enriched sample (b), or from a pure $W+$ light partons MC sample (c).

The functional form chosen here for $S(M_T)$ is a Crystal Ball function [42]:

$$S(M_T) = N \cdot G(M_T|m,\sigma)\,, \quad \text{for } \tfrac{M_T-m}{\sigma} > -\alpha\,, \tag{4}$$

$$S(M_T) = N \cdot A \cdot \left(B - \frac{M_T - m}{\sigma}\right)^{-n}\,, \quad \text{for } \tfrac{M_T-m}{\sigma} \leq -\alpha\,, \tag{5}$$

$$\tag{6}$$

where N, α, n, m and σ are the free parameters of the fit, and

$$A = \left(\frac{n}{|\alpha|}\right)^n \cdot exp\left(-\frac{|\alpha|^2}{2}\right)\,, \tag{7}$$

$$B = \frac{n}{|\alpha|} - |\alpha|\,; \tag{8}$$

all the parameters are constrained to positive values in order to avoid pathological fits, and the peak m of the Gaussian $G(M_T|m,\sigma)$ intended to model the high-M_T region is constrained to the $[60, 150]$ GeV range in order to make sure that it will not be too far away from the M_W value.

The prediction for QCD contamination in the signal region is calculated as $b \cdot \int_{50\ \text{GeV}}^{\infty} B(M_T) dM_T$. The final result in this study is based on the $B(M_T)$ shape extracted from the QCD-enriched sample, and the $S(M_T)$ shape extracted in three complementary ways:

- from the Z-enriched control sample, see Fig. 10(a), predicting 22.0 events in the signal region (i.e., the

Fit parameter	Z-enr. plus QCD-enr.	W-enr. plus QCD-enr.	pure $W+$ light partons plus QCD-enr.
p_0	4,432 $\pm$ 27	same	same
p_1	-610.8 $\pm$0.4	same	same
p_2	-13.934$\pm$0.005	same	same
p_3	$(291.47 \pm 0.05) \times 10^{-3}$	same	same
p_4	$(-135.43 \pm 0.04) \times 10^{-5}$	same	same
N	201 ± 7	$2{,}248 \pm 22$	$2{,}236 \pm 22$
α	1.36 ± 0.21	0.52 ± 0.04	1.04 ± 0.07
n	1.18 ± 0.83	0.31 ± 0.06	0.72 ± 0.16
m	72.0 ± 0.6 GeV	69.7 ± 0.4 GeV	70.5 ± 0.3 GeV
σ	20.1 ± 0.6 GeV	23.3 ± 0.3 GeV	22.3 ± 0.3 GeV
a	0.19 ± 0.01	$(1.61 \pm 0.10) \times 10^{-2}$	$(1.63 \pm 0.10) \times 10^{-2}$
b	$(1.70 \pm 0.10) \times 10^{-3}$	$(1.17 \pm 0.10) \times 10^{-3}$	$(1.53 \pm 0.10) \times 10^{-3}$
Prediction	22.0	15.1	19.7

Table 8: Fit parameters in the three complementary QCD extraction scenarios for $B(M_T)$ $(p_0, \cdots, p_4)$, $S(M_T)$ $(N, \alpha, n, m, \sigma)$, and $F(M_T)$ (a, b), and final predictions of the QCD contamination in the signal region ($M_T > 50$ GeV).

$M_T > 50$ GeV range). The statistical uncertainty on the parameter b of Eq. 3, which corresponds to the scale of the QCD contribution, is $\pm 5.9\%$;

- from the W-enriched control sample, see Fig. 10(b), predicting 15.1 events, and $\Delta b/b = \pm 8.5\%$;
- from the pure $W+$ light partons Monte Carlo sample with no b tagging, Fig. 10(c), yielding a prediction of 19.7 events, and $\Delta b/b = \pm 6.5\%$.

All these predictions have to be compared with 12 ± 7 actual QCD events.

The satisfactory closeness of all the three final predictions to each other, despite the different $S(M_T)$ shapes, is attributed to the fact that the most critical element in the fit are: the $B(M_T)$ shape (here the same in all three cases), and the Gaussian part of $S(M_T)$. Table 8 shows the results of the $S(M_T)$ fits for the three samples, and it is apparent that the m and σ parameters, modeling the shape in the signal region, tend to converge towards the same values, while the α and n parameters, most important in the QCD-dominated region, are quite different in the three cases.

We conclude that the spread in results coming from the different $S(M_T)$ extractions dominates over the purely statistical uncertainty from the fit ($\Delta b/b$), but all the predictions reasonably agree with the actual count of events. Although not very precise, this method makes sure that we don't make an order-of-magnitude mistake on the QCD estimation.

In the rest of the note we will use the event yield predicted with this procedure when using $S(M_T)$ taken from the Z-enriched sample (22 events), assigning to it a 40% uncertainty (i.e., around 9 events), roughly corresponding to the maximum distance of the results (7 events) divided by their average.

5 Top quark reconstruction

Once a supposedly signal-enriched sample has been selected from real collision data, it is important to check that it exhibits the features expected for single top. The most obvious is the presence of a top quark, recognizable from a mass peak when properly combining the final state objects. Another useful feature, exploitable after the reconstruction of the top quark, is the angular distribution of the lepton, related with the top-quark polarization which is a specific feature of the electroweak mode of production and thus of our signal. Both will have a central role in the signal extraction technique described in Sec. 6, and both require the reconstruction of a top quark candidate.

5.1 W mass constraint

The first step in the reconstruction of the top quark from its decay products is the reconstruction of the W boson. Since this analysis considers only muonic decays of this boson, we must assume that the x and y components of

Assignment	Fraction
b-tagged jet is b from top quark	92.2%
b-tagged jet is second b	4.0%
b-tagged jet is the recoil light quark	0.1%
b-tagged jet is none of the above	3.7%
untagged jet is b from top quark	1.2%
untagged jet is second b	1.6%
untagged jet is the recoil light quark	87.2%
untagged jet is none of the above	10.0%

Table 9: Matching of the b-tagged and untagged jets to MC truth, in selected signal events, for $\Delta R(jet, parton) < 0.3$.

the missing energy (properly corrected) are entirely due to the escaping neutrino, and apply the W-mass constraint in order to extract the z component ($P_{z,\nu}$):

$$M_W^2 = (E_\mu + \sqrt{\not{E}_{\rm T}^2 + P_{z,\nu}^2})^2 - (\vec{P}_{T,\mu} + \vec{\not{E}}_{\rm T})^2 - (P_{z,\mu} + P_{z,\nu})^2 \ . \tag{9}$$

This equation has in general two solutions:

$$P_{z,\nu}^{A,B} = \frac{\mu \cdot P_{z,\mu}}{P_{T,\mu}^2} \pm \sqrt{\frac{\mu^2 \cdot P_{z,\mu}}{P_{T,\mu}^4} - \frac{E_\mu^2 \cdot \not{E}_{\rm T}^2 - \mu^2}{P_{T,\mu}^2}} \ , \tag{10}$$

with

$$\mu = \frac{M_W^2}{2} + \vec{P}_{T,\mu} \cdot \vec{\not{E}}_{\rm T} \ . \tag{11}$$

5.1.1 Complex solutions

If the discriminant in equation 10 becomes negative, or equivalently M_T is larger than the W pole mass used in the constraint, the solutions have an imaginary part. This happens in 36.0% of the cases, mostly due the finite resolution of $\not{E}_{\rm T}$ (lepton momentum resolution and the finite W width give negligible contributions; see, e.g., the s-channel single-top analysis in Ref. [52] for a detailed study of this effect in very similar conditions).

Several schemes exist to deal with this situation; here the imaginary component is eliminated by modifying $\not{E}_{\rm T}$ such to give $M_T = M_W$, still respecting Eq. 9. This is obtained by imposing that the discriminator, and thus the square root in Eq. 10, are null; this gives a quadratic relation between $P_{x,\nu}$ and $P_{y,\nu}$, with two solutions, among which the one with minimal distance between $P_{T,\nu}$ and $\not{E}_{\rm T}$ is chosen.

5.1.2 Ambiguity resolution and event interpretation

In the "normal" case of two real solutions for $P_{z,\nu}$, different choice criteria have been proposed in the literature. Here we choose the solution with the smallest absolute value. The W boson is thus reconstructed by this procedure when the discriminant of Eq. 10 is positive, and by the procedure of the preceding section when it is negative. A similar two-fold ambiguity presents when reconstructing a top-quark hypothesis, since two jets are selected. The ambiguity is resolved by assigning the b-tagged jet to the top-quark decay.

The b-tagged jet matches the true b quark from top-quark decay in 92.2% of the selected signal events, using as matching criterion a distance of $\Delta R < 0.3$ from the parton; more details are given in Table 9.

5.2 Reconstructed top-quark mass

Figure 11 shows the mass of the reconstructed top quark ($M_{l\nu b}$) for events passing the full selection. The observation of a peak at $\approx M_{top}^{Tevatron}$ in the selected sample from real collision data will be a smoking gun of the presence of top quarks.

For QCD and $W/Z + X$ events, $M_{l\nu b}$ tends to be broad and soft. In $t\bar{t}$ events, a peak is present but it is broadened with respect to the signal by several effects, e.g.: two true b quarks are present, and in 50% of cases we expect to pick up the one not coming from the same top as the selected muon; and in $t\bar{t} \to 2l$ events (including tauons) the missing energy gets contributions by more than one neutrino.

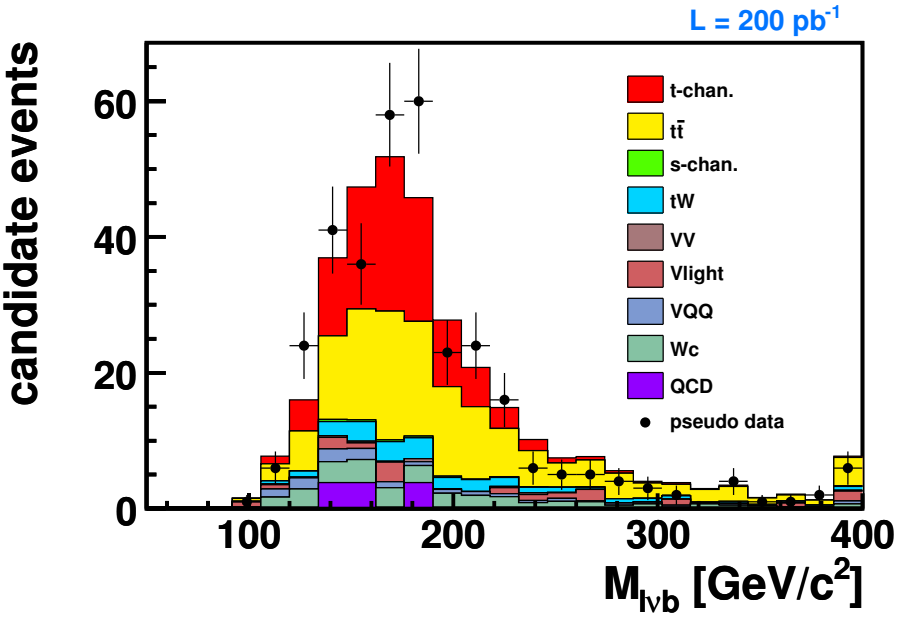

Figure 11: Reconstructed top-quark mass after full selection.

5.3 Top quark polarization angle

A specific feature of our signal, stemming from the $V-A$ structure of the weak interaction, is the almost 100% left-handed polarization of the top quark with respect to the spin axis [47]. The direction of the top quark spin is reflected in angular correlations in its decay products, which are distributed according to the formula

$$\frac{1}{\Gamma}\frac{d\Gamma}{d\cos\theta^*} = \frac{1}{2}(1 + A\cos\theta^*)\,, \tag{12}$$

where θ^* is the angle between the direction of the outgoing particle and the spin axis, in the top-quark rest frame. A is a coefficient of spin asymmetry, which depends on the identity of the particle and is equal to $+1$ for charged leptons [47].

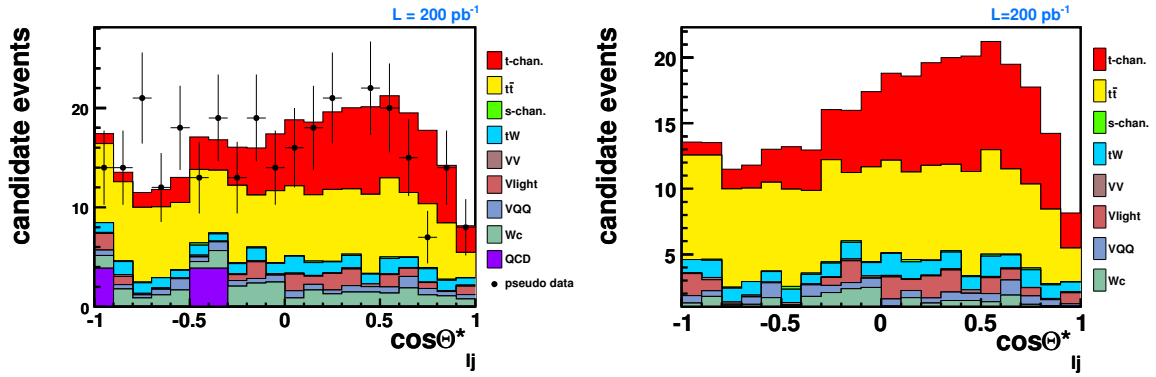

Figure 12: Cosine of the angle between charged muon and untagged jet in the reconstructed top rest frame after full selection, for all processes (a) and without QCD (b).

We make use of the "spectator basis" (see, e.g., Ref. [48]), where θ^* is taken equal to the angle θ^*_{lj} between the muon direction and the light quark recoiling against the virtual W boson, in the top-quark rest frame; in practice, the direction of the untagged jet is chosen as spin axis, after a boost of all the 4-vectors is performed in the rest frame of the reconstructed top quark.

The dip at $\cos\theta^*_{lj} \approx 1$ is an artifact of the muon selection. For this reason in Sec. 6.3.2 we limit our use of this variable to the $[-1, 0.75]$ interval. The same artifact, and the sensitivity of the shape of this variable to some

modeling effects, have been studied at generator level in Ref. [49].

6 Signal extraction and cross section measurement

Two separate binned likelihood fits are performed to the distributions of $M_{l\nu b}$ and $\cos\theta^*_{lj}$ to determine the single top cross section. The sensitivities of the two measurements are computed using ensemble tests. The statistical technique used in this text has been already applied in CDF searches of single top [5, 50].

6.1 Binned likelihood function

The likelihood function is given by:

$$L(\beta_1, \ldots, \beta_{C'}, \ldots \beta_C) = \prod_{k=1}^{B} P(n_k|\mu_k) \cdot \prod_{j=2}^{C'} G(\beta_j|1, \Delta_j) \; ; \tag{13}$$

where B is the number of bins, k the bin index, C is the number of processes (including signal), and j is the process index. The signal process is labeled with $j = 1$, the background processes have indices from $j = 2, ..., C$. Background processes from $j = 2$ to $j = C'$ are constrained, while background processes with $C' < j \leq C$ are unconstrained. Here $\beta_j = \nu_j/\hat{\nu}_j$ represents the ratio of the measured number of events ν_j and the predicted number of events $\hat{\nu}_j$ for process j. Therefore, β_j can be interpreted as the ratio of the measured and the predicted cross section for process j. The parameter of interest is β_1 (also indicated as β_{signal}), which indicates the ratio of the measured single top cross section and the predicted single top cross section. The Δ_j are the relative uncertainties on the predicted number of background processes.

The first term, $P(n_k|\mu_k)$, of Eq. 13 is the Poisson distribution of the observed number n_k of selected events per bin k:

$$P(n_k|\mu_k) = \frac{\mu_k^{n_k}}{n_k!} \cdot e^{-\mu_k} \; , \tag{14}$$

where μ_k is the expectation value of the distribution in bin k, taken as the sum of the expectations for signal and backgrounds for that specific bin,

$$\mu_k = \sum_{j=1}^{C} \mu_{jk} = \sum_{j=1}^{C} \beta_j \cdot \hat{\nu}_j \cdot \alpha_{jk} \; , \tag{15}$$

where α_{jk} is the content of bin k of the normalized histogram of the chosen sensitive observable for process j, i.e., $\sum_{k=1}^{B} \alpha_{jk} = 1, \; \forall j$.

The second term of Eq. 13 is a Gaussian constraint centered on 1 and with standard deviation Δ_j, used for some backgrounds:

$$G(\beta_j|1, \Delta_j) = \frac{1}{\sqrt{2\pi}\Delta_j} \cdot exp\left(\frac{-(\beta_j - 1)^2}{2\Delta_j^2}\right) \; ; \tag{16}$$

hence, the event rates for some background processes are constrained to the values foreseen from theory or from an independent estimation (the one from Sec. 4 in the QCD case), within their relative uncertainty Δ_j.

The negative logarithm is simultaneously minimized for all free parameters, the β_j. This yields not only β_1 for the signal but also the β_j ($j \geq 2$) for the background processes. The minimization is performed using the MINUIT [51] package.

In order to compute the sensitivity of the analysis two different ensemble tests are performed, one including single top-quark events (hypothesis H_1) and one without any single top-quark events (hypothesis H_0). An ensemble test consists of a set of simulated, so-called pseudo experiments. For each of these pseudo experiments the number of events N_j of an unconstrained process is drawn from a Poisson distribution of mean $\hat{\nu}_j$, while the number of events of a constrained process are drawn according to a Gaussian with mean $\hat{\nu}_j$ and width $\hat{\nu}_j \cdot \Delta_j$. For each pseudo experiment and for both ensemble tests (H_0 and H_1) the Q-value is determined:

$$Q = -2 \ln \left(\frac{L(\hat{\beta}_1, \hat{\beta}_2, \ldots, \hat{\beta}_C)}{L(\beta_1 = 0, \tilde{\beta}_2, \ldots, \tilde{\beta}_C)} \right) \tag{17}$$

Here, the hat-symbol indicates the minimized values of a fit with all parameters, and the tilde-symbol represents the minimized values if only the background parameters have been fitted, while the signal contribution was fixed to zero. The Q-value distribution for the H_0 hypothesis is q_0, the Q-value distribution for H_1 is q_1. The probability for H_0 to be true can be stated with the p-value, defined by:

$$p(Q_m) = \frac{1}{A_q} \cdot \int_{-\infty}^{Q_m} q_0(Q')\, dQ' \ , \tag{18}$$

where $A_q = \int_{-\infty}^{\infty} q_0(Q')\, dQ'$ and Q_m is the Q-value, in case of observed events, or the median of the q_1 distribution, in case of pseudo experiments. The meaning of this expected p-value ($\hat{p}$) is the following: under the assumption that H_1 is true, one expects to observe $p < \hat{p}$ with a probability of 50%. The sensitivity σ of the analysis is related to the p-value by:

$$\sigma = \sqrt{2} \cdot Erf^{-1}(1 - 2(1-p)) \ , \quad \text{with} \quad Erf(z) = \frac{2}{\pi} \int_0^z e^{-t^2}\, dt \tag{19}$$

6.2 Template extraction

Templates are built *in situ* for groups of similar processes from control samples with enlarged statistics, with the only exception of single top in all channels, for which the use of Monte Carlo seems to be the only option in this scenario.

Single top in the s channel has a shape similar to t channel in both $M_{l\nu b}$ and $\cos\theta^*_{lj}$, see Fig. 13(a) and Fig. 14(a); thus, it is considered as a signal component in the fit, to be later subtracted according to the σ_s/σ_t ratio predicted by the Standard Model. A dedicated measurement of σ_s, able to separate these two single-top components, will have to wait until a much larger statistics and a better control of systematics will be available, as indicated by a previous study [52]. The template for t- plus s- channel single top is taken from Monte Carlo.

Similar background spectra are combined into one distribution, too:

- the QCD template is taken from the b-tag-less anti-isolated sample discussed in Sec. 4, see Table 5 and Fig. 9(left), with the addition of the $M_T > 50$ GeV cut; the comparison with a sample with $relIso > 0.95$ is shown in Fig. 15;
- events of the $W+X$ family tend to be similar to each other and to $Z+X$, see Figs. 13(c,d) and Figs. 14(c,d); the combined $W/Z + X$ template is taken from the W-enriched sample already discussed in Sec. 4, see Table 6 and Fig. 9(center), with the addition of the $M_T > 50$ GeV cut; the comparison with the standard selection is shown in Fig. 16 for $W + X$ events;
- the $M_{l\nu b}$ and $\cos\theta^*_{lj}$ shapes are similar for $t\bar{t}$ and tW, see Fig. 13(b) and Fig. 14(b); the $t\bar{t} + tW$ template is taken from Monte Carlo.

No specific template has been considered for WW, WZ, ZZ events, due to the smallness of their contamination and their resemblance with the $W/Z + X$ family.

In the control samples with no b tagging, the role of the b jet is taken by the most central jet in the event.

The templates obtained this way for the $M_{l\nu b}$ and $\cos\theta^*_{lj}$ variables are shown in Fig. 17(a) and (b) respectively. It can be seen that in the $\cos\theta^*_{lj}$ case the templates deviate very little from flatness, with the exception of QCD which is anyway a relatively minor contamination, and can be in principle subtracted after the specific estimation presented in Sec. 4; thus, in Sec. 6.3.2 we will use a flat distribution as standard template for the overall background, and we will consider the observed deviation from flatness of these templates as robustness tests in Sec. 7.6.

The flatness in $\cos\theta^*_{lj}$ of the $t\bar{t}$ events, which is a crucial assumption of the fit on this variable, is tested by a control sample corresponding to the events failing the second b veto. The event yield of this orthogonal selection is shown in Table 10, and Fig. 18 shows the $\cos\theta^*_{lj}$ shape for this sample. In order to test the flatness we need to correct for the residual presence of signal, and we propose to do this by an iterative procedure: the result of the full signal extraction will be used to estimate the signal contamination in this sample, and its contribution will be subtracted.

6.3 Likelihood fit

The likelihood function, Eq. 13, is fitted by minimizing its negative logarithm with respect to $\beta_1, \ldots, \beta_C$.

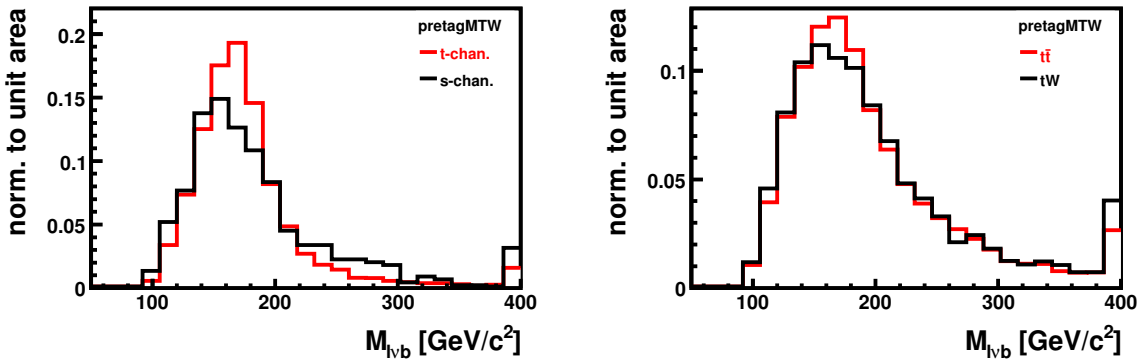

(a)

(b)

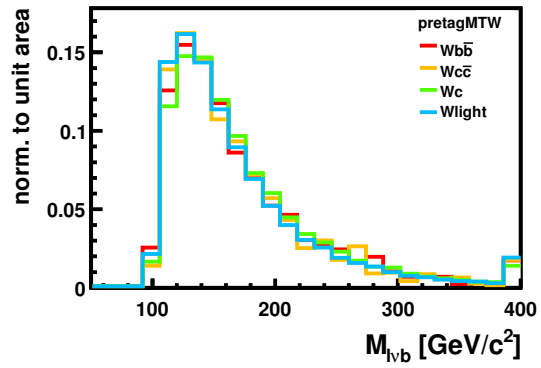

(c)

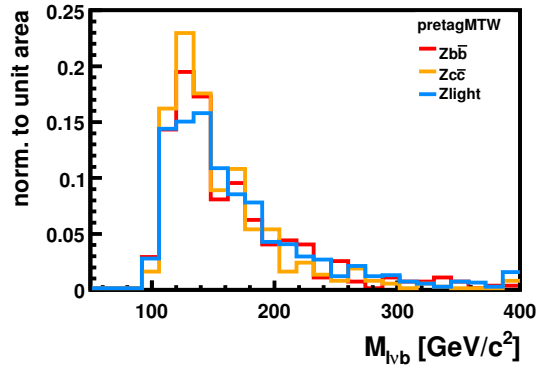

(d)

Figure 13: Comparison of the $M_{l\nu b}$ shapes for t and s channel (a), $t\bar{t}$ and tW (b), $W + X$ (c), $Z + X$ (d). The comparison is performed for a selection without b tagging and M_T cut, in order to enhance the statistics.

We estimate the statistical sensitivity of the signal extraction by simulating 500,000 pseudoexperiments, and plotting an histogram of the outcomes for β_1. We expect this distribution to peak close to 1, and the root mean square of the distribution is taken as an estimation of the statistical uncertainty.

6.3.1 Fit to $M_{l\nu b}$

The following fitting scenarios are considered:

- S_1: signal and $W/Z + X$ are kept free in the fit[1)], while QCD and $t\bar{t} + tW$ are fluctuated within $\pm 40\%$ and $\pm 20\%$ of the nominal values respectively;
- S_2: as S_1, but $W/Z + X$ is also constrained, by $\pm 50\%$ of the nominal value.
- S_3: as S_1, but $t\bar{t} + tW$ is constrained within $\pm 50\%$ of the nominal value.
- S_4: as S_1, but $t\bar{t} + tW$ is unconstrained.

The values used for the Gaussian constraints will be justified in Sec. 6.4.

[1)] Profiling (see Sec. 6.1) is performed on backgrounds even if unconstrained.

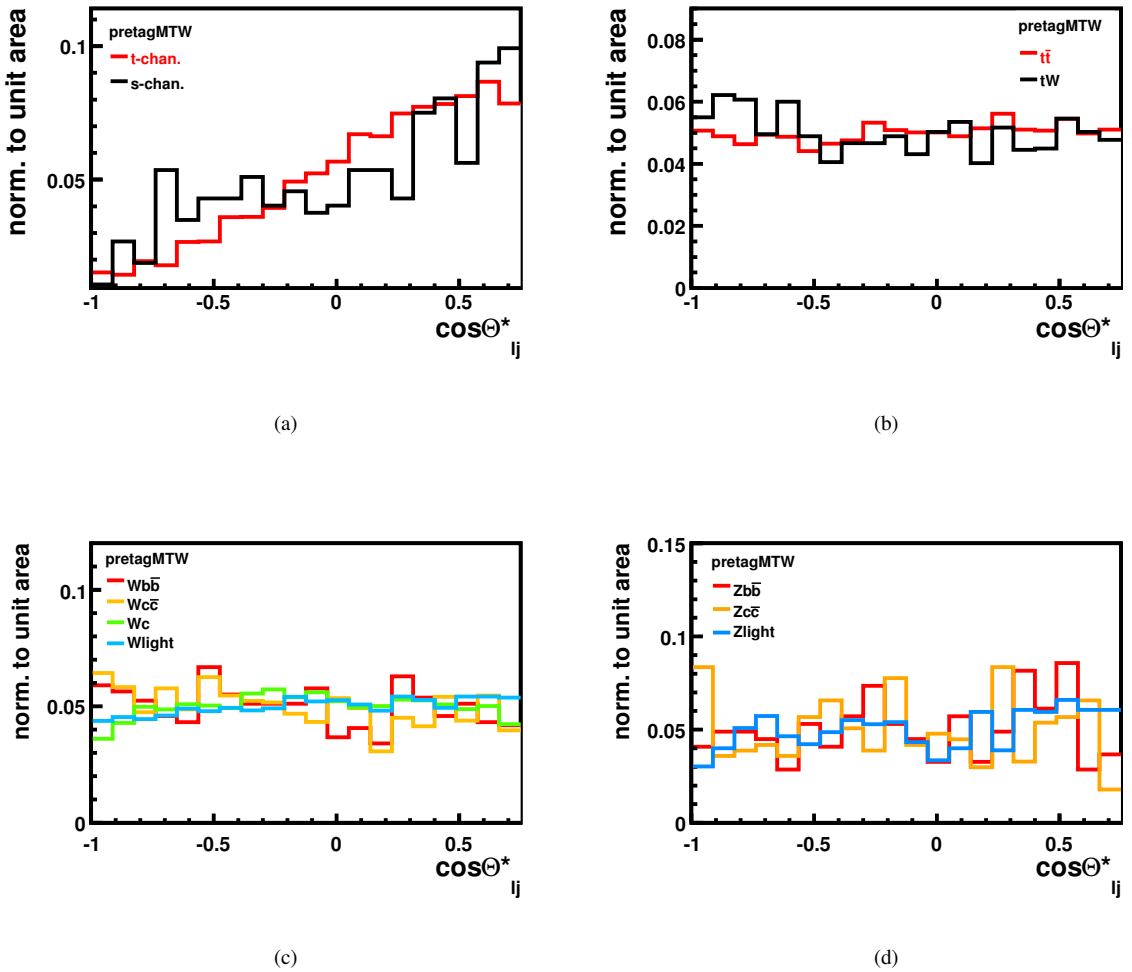

Figure 14: Comparison of the $\cos\theta^*_{lj}$ shapes for t and s channel (a), $t\bar{t}$ and tW (b), $W+X$ (c), $Z+X$ (d). The comparison is performed for a selection without b tagging and M_T cut, in order to enhance the statistics.

6.3.2 Fit to $\cos\theta^*_{lj}$

The fit is restricted to the $[-1, 0.75]$ interval, i.e., the region of linear rise, for two reasons: to reduce the sensitivity to all the modelling details affecting isolation and other aspects of the muon selection, and to permit the template extraction from non-isolated or anti-isolated control samples.

Our standard fitting scenario is the following:

- S_{flat}: a flat template is assumed for the sum of the backgrounds, and the overall background level is kept free in the fit.

In addition we also consider scenarios S_1 and S_2, defined as in the $M_{l\nu b}$ case.

6.4 Gaussian constraints for backgrounds

In the fitting scenarios outlined in Sec. 6.3.1 where a Gaussian constraint is used, we have to assume an uncertainty separately for different background component. This task is especially hard since we assume to perform this measurement at a time when the early LHC collisions will have just started to be digested. The reader must be aware that the following list contains much guesswork:

- $t\bar{t}$: the single-muonic analysis with no b tagging will reach a $\pm 10\%$ uncertainty very soon [43], then the Jet

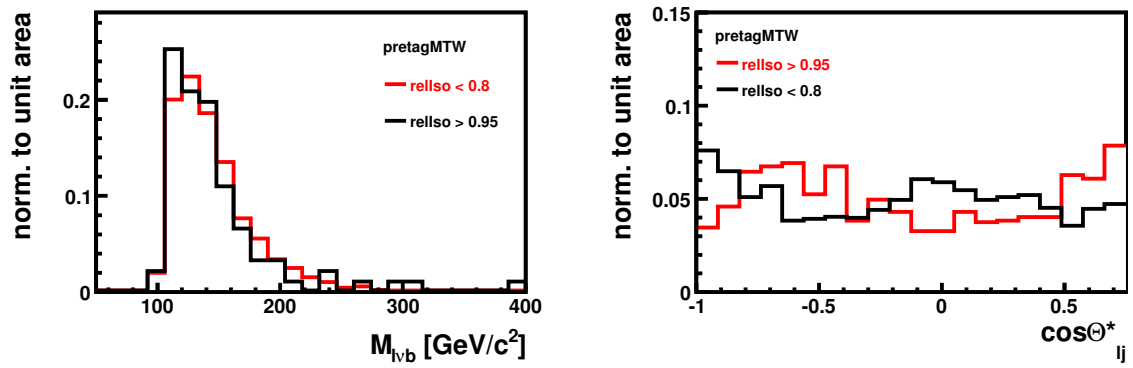

(a) (b)

Figure 15: Comparison between QCD events with anti-isolation and standard isolation, for $M_{l\nu b}$ and $\cos\theta^*_{lj}$ shapes.

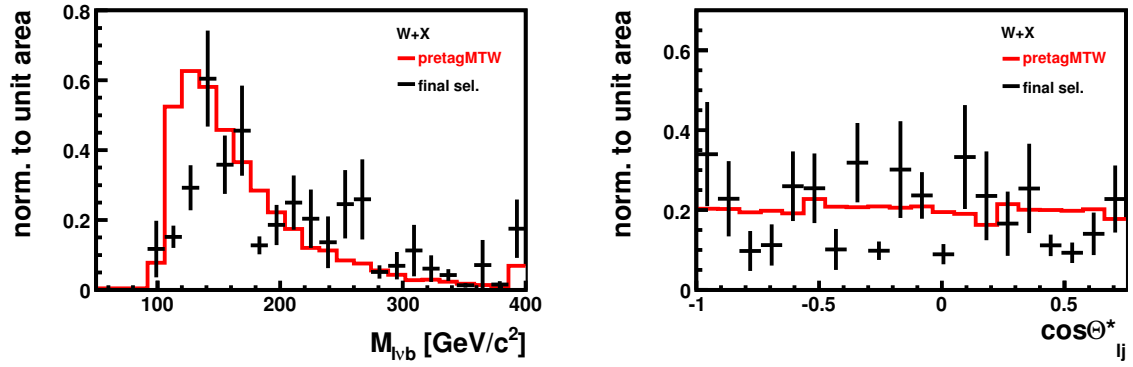

(a) (b)

Figure 16: Comparison between $W + X$ events with and without b-tagging requirements, for $M_{l\nu b}$ and $\cos\theta^*_{lj}$ shapes.

Energy Scale uncertainty is expected to become the dominant error[2)], but we don't consider it here in order to avoid double counting with our own estimation, Sec. 7.2. Other systematic uncertainties have not been studied at the moment of writing this note. Here we apply a $\pm 20\%$ (S_1, S_2) or 50% (S_3) variation on this process, when it is not unconstrained in the fit (S_4). The tW variation is bound to the $t\bar{t}$ one.

- $W/Z + jets$ and $W/Z + Q\bar{Q}$: the most important issues from the point of view of our analysis are the radiation modeling, affecting the number of jets with a chance to pass the p_T threshold, and the heavy flavour fraction; both of them will require much work to be extracted from data. Here we keep them free in the fit (S_1, S_3, S_{flat}) or apply a 50% uncertainty (S_2), and we test the robustness of the analysis against scale factors of 2 and 3.

- QCD: its a priori uncertainty is probably the worst, because it only passes the selection through the very extreme tails of the distributions, but it will be very abundantly produced in pp collisions and we illustrated in Sec. 4 our strategy to constrain it. Our method, applied to the present selection, yields a 40% spread

[2)] The method of fitting the reconstructed top mass is expected to yield a cross section uncertainty of $\approx \pm 10\%$ for $\pm 10\%$ error on JES [44].

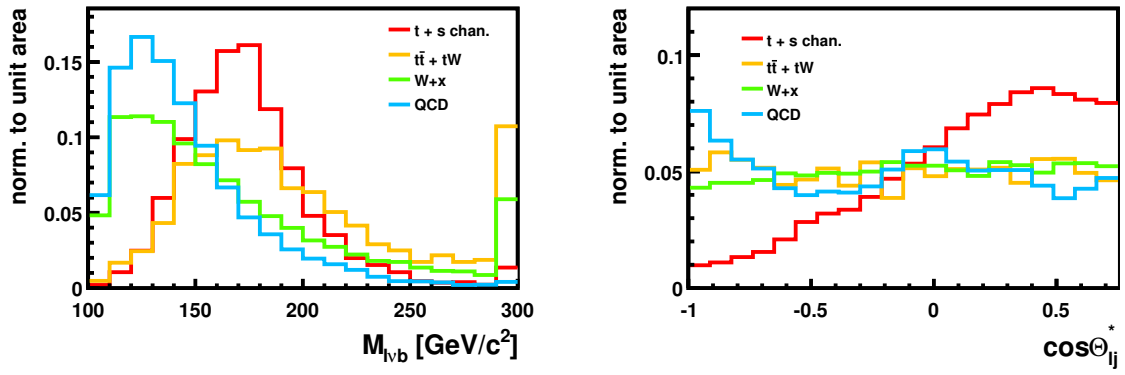

(a) (b)

Figure 17: Templates for $M_{l\nu b}$ (a) and $\cos\theta^*_{lj}$ (b) shapes.

Process	N_{evt} in MC	N_{evt} in 200 pb^{-1}
t-channel	705	20.8
s-channel	107	2.9
tW	191	6.6
$t\bar{t}$	1016	92.9
QCD	1	3.9
$Wb\bar{b}$	134	9.3
$Wc\bar{c}$	13	0.6
Wc	40	4.
$W+$ light partons	5	4.2

Table 10: Event yield for the main processes in the $t\bar{t}$-enriched selection constituted by events failing the second b veto.

between the three complementary results, and we use this in the Gaussian constraint in all scenarios apart from S_{flat}.

Table 11 summarizes this list for fitting scenario S_1, i.e., our standard one for $M_{l\nu b}$.

6.5 Fit results

Figure 19 shows the β_1 distributions for $M_{l\nu b}$ and $\cos\theta^*_{lj}$ in the S_1 and S_{flat} scenarios respectively. Table 12 compares σ_β and the expected statistical sensitivities in all the fitting scenarios.

The linearity of the fit is checked in Fig. 20 for both $M_{l\nu b}$ and $\cos\theta^*_{lj}$ fits and Fig. 21 shows the evolution of the relative cross-section error with the integrated luminosity.

7 Systematic uncertainties and robustness tests

This section considers the sensitivity of the analysis to systematic uncertainties of instrumental or physics origin, as well as the effect on the results when very extreme variations are applied to the underlying assumptions.

Process	Uncertainty
$t\bar{t}$	$\pm 20\%$
$W/Z + X$	$\pm 50\%$
QCD	$\pm 40\%$

Table 11: Widths of the Gaussian constraints of the background samples in the S_1 fitting scenario.

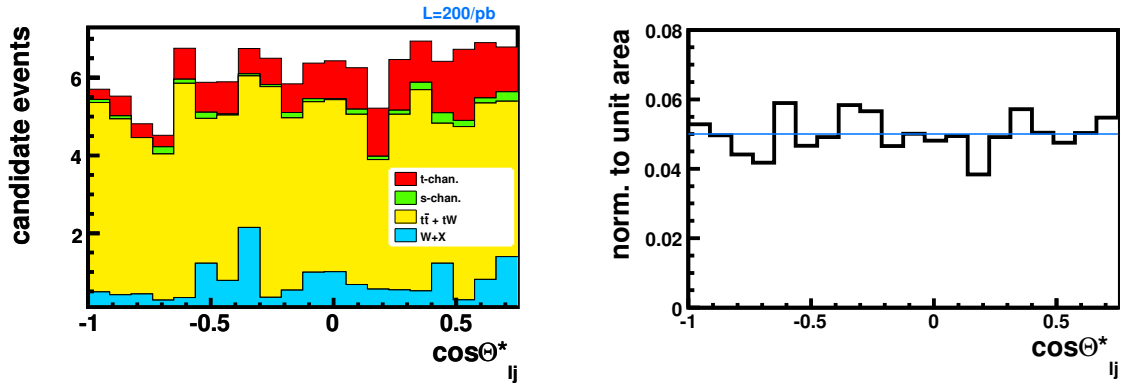

(a) (b)

Figure 18: Distribution of $\cos\theta^*_{lj}$ for events failing the second b veto, as expected in 200 pb^{-1} of data (a), and for $t\bar{t}$ only (b).

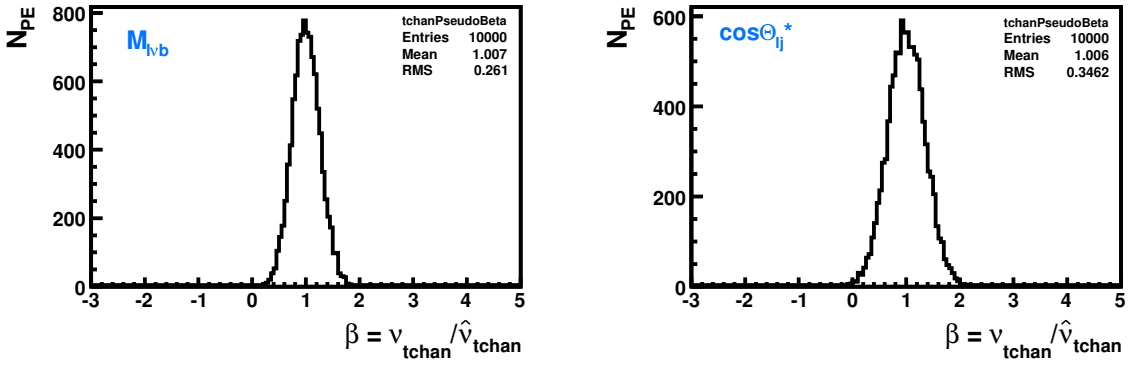

(a) (b)

Figure 19: Distribution of the outcome of 10,000 pseudo-experiments from $M_{l\nu b}$ in the S_1 scenario (a) and $\cos\theta^*_{lj}$ in the S_{flat} scenario (b).

7.1 Parton Distribution Functions uncertainty

The impact of PDF uncertainty on this measurement is estimated by reweighting the selected events and observing the variations in the event yields and on the $M_{l\nu b}$ and $\cos\theta^*_{lj}$ shapes. Each selected event is assigned a different weight for each available PDF eigenvector in the CTEQ61 collection [18], following the recipe in Ref. [45]. It can be argued that this result is conservative, since it assumes that the PDF uncertainty at the time when 200 pb^{-1} will have been acquired and fully analyzed will be the same as at the moment of writing this note, while many LHC measurements with the potential to constrain the PDF uncertainty (see, e.g., Ref. [46]) require relatively small amounts of data before being competitive with the current constraints extrapolated from lower-energy experiments.

We observe in Fig. 22 that the deviations from the default value are dominated by one eigenvector in the positive and one in the negative direction. Sets n.28 and n.29 in the CTEQ61 collection are the PDF eigenvalues yielding the maximum upward ($+5.8\%$) and maximum downward (-4.5%) variations for signal, while sets n.8 and n.9 are the most extreme for both $t\bar{t}$ and tW; see Fig. 23 for the effect on $M_{l\nu b}$ and $\cos\theta^*_{lj}$ shapes. Since our procedure to extract the cross section is quite time-consuming due to the use of many pseudo experiments, here we choose to approximate the systematic uncertainty from PDF by taking only the eigenvectors of maximum rate variation for signal, $t\bar{t}$, and tW respectively. All the other backgrounds are kept unvariated, since we don't have enough MC

$M_{l\nu b}$ fit	S_1	S_2	S_3	S_4
σ_β	0.26	0.25	0.30	0.31
Expected sensitivity	3.5σ	3.9σ	3.2σ	2.9σ

$\cos\theta^*_{lj}$ fit	S_1	S_2	S_{flat}
σ_β	0.39	0.31	0.34
Expected sensitivity	2.4σ	3.1σ	2.8σ

Table 12: Outcome of the fits for $M_{l\nu b}$ and $\cos\theta^*_{lj}$, with 500,000 pseudoexperiments.

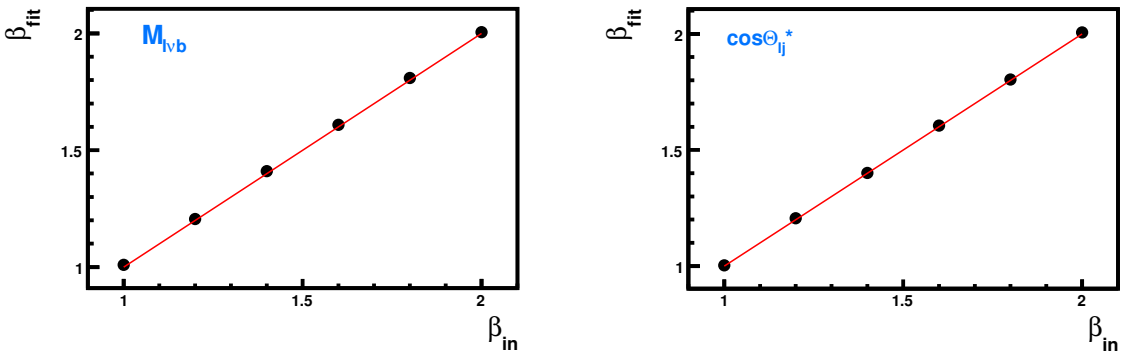

(a) (b)

Figure 20: Linearity check for $M_{l\nu b}$ in scenario S_1 (a) and $\cos\theta^*_{lj}$ in scenario S_{flat} (b).

statistics to extract meaningful variations after full selection.

7.2 Jet Energy Scale (JES) and $\not{E}_{\rm T}$ scale uncertainty

In a scenario with more than ≈ 100 pb^{-1} of data on tape, from data-driven methods to extract jet calibrations we expect a JES uncertainty of $\approx \pm 10\%$ [35]. In this analysis we apply a simultaneous variation of $1+\alpha$ on all jet 4-momenta, where α can take the values $+10\%$ and -10%.

Since $\not{E}_{\rm T}$ has "Type I" corrections, i.e., the calorimetric clusters associated to jets are given the calibrated jet momenta, its uncertainty is correlated with the JES uncertainty.

Here two independent sources of $\not{E}_{\rm T}$ systematics are considered:

- correlated with JES: all the jets above 20 GeV are corrected by the same factors discussed before, and $\not{E}_{\rm T}$ is recalculated accordingly;
- uncorrelated with JES: after subtracting the jet corrections, $\not{E}_{\rm T}$ is variated by $\pm 10\%$.

The impact on the shapes of $M_{l\nu b}$ and $\cos\theta^*_{lj}$ is shown in Figs. 24 and 25 for JES and $\not{E}_{\rm T}$ rescalings respectively.

7.3 b tagging and mistagging uncertainties

For the tight and loose b-tagging working points used in this analysis, respectively for the tagged and veto jets, estimates of the expected uncertainty for the efficiencies of true and fake b-jets identification can be found, respectively, in Refs. [37] and [38], in different integrated luminosity scenarios (10, 100, 1000 pb^{-1}). For the 100 pb^{-1} case, the b-tagging efficiency for the track-counting algorithm is expected to be known within $\pm 8.0\%$ ($\pm 8.2\%$) for the tight (loose) working point, while for mistagging the uncertainty is expected to be $\pm 18.1\%$ ($\pm 3.4\%$) for the tight (loose) working point.

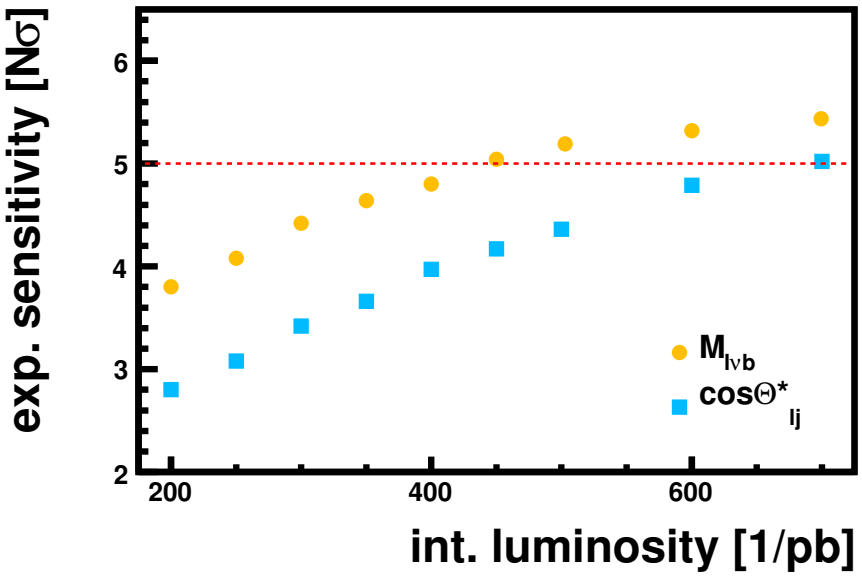

Figure 21: Evolution of the expected sensitivity with the integrated luminosity for $M_{l\nu b}$ and $\cos\theta^*_{lj}$.

These uncertainties have been translated into variations of the b-tagging discriminator, selecting from MC truth the taggable jets associated or not to real b quarks in signal events. This procedure gives a $[4.87-5.91]$ ($[0.87-2.12]$) range around the 5.36 (1.47) threshold for tight (loose) selection when considering real b quarks, and a $[5.01-5.91]$ ($[1.45-1.48]$) range when considering mistags. The thresholds for the tight and loose selections are taken 100% correlated, while tagging and mistagging errors are considered uncorrelated, as they come from independent data-driven measurements.

The impact on the $M_{l\nu b}$ and $\cos\theta^*_{lj}$ shapes is negligible, as shown in Figs. 26 and 27 for the efficiency and mistagging variations respectively.

7.4 Signal modeling

As explained in Sec. 2, we model the signal by matching the $2\to2$ and $2\to3$ diagrams at Leading Order, and we normalize to the NLO cross section.

In order to maximize the effect of parton-level signal modeling, we compare the $M_{l\nu b}$ and $\cos\theta^*_{lj}$ shapes for the $2\to2$ and the $2\to3$ components separately. We expect this to be by far an overestimation of the modeling uncertainty.

In the $\cos\theta^*_{lj}$ case no deviation from the matched sample is noticeable, nevertheless a small effect is seen on the expected sensitivity of the fit when the $2\to3$ template is considered. This is attributed to statistical fluctuations of the small $2\to3$ sample currently available, thus this effect is not considered in the overall systematic uncertainty.

7.5 $t\bar{t}$ modeling

In order to assess the sensitivity to Initial/Final State Radiation (ISR/FSR), three samples have been produced with the CMS fast simulation (FastSim) [53]:

- a reference sample generated with the central settings suggested in Ref. [54];
- a sample with higher radiation probability;
- a sample with lower radiation probability;

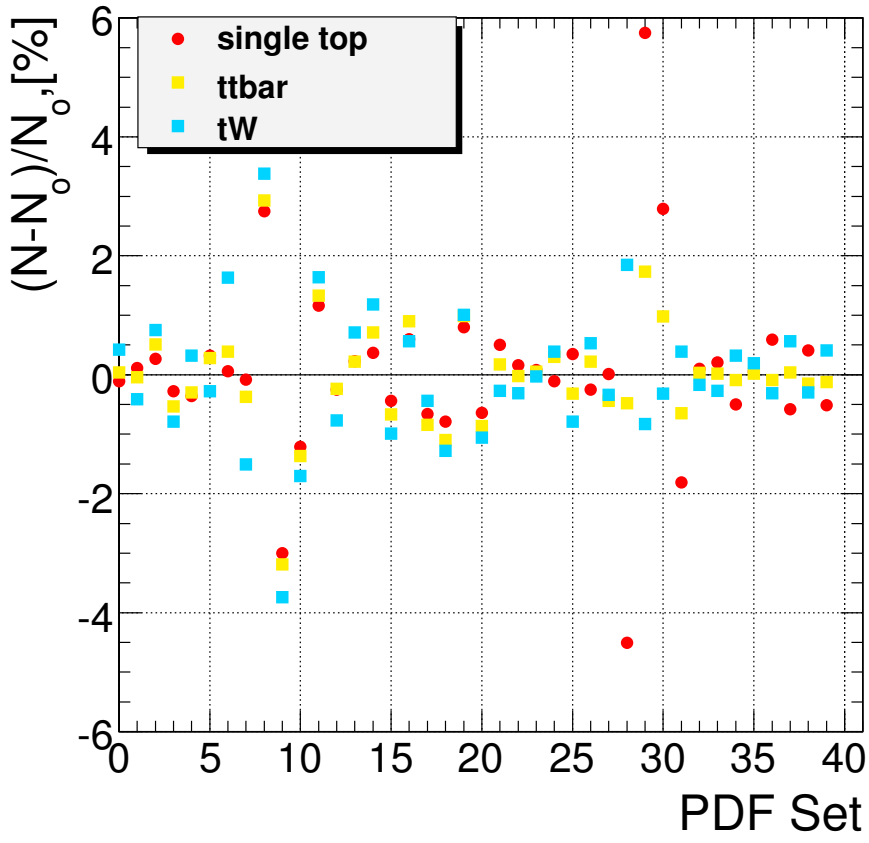

Figure 22: Relative variation (in %) of the selection efficiencies for signal, $t\bar{t}$, and tW, versus the PDF-set index in the CTEQ61 collection.

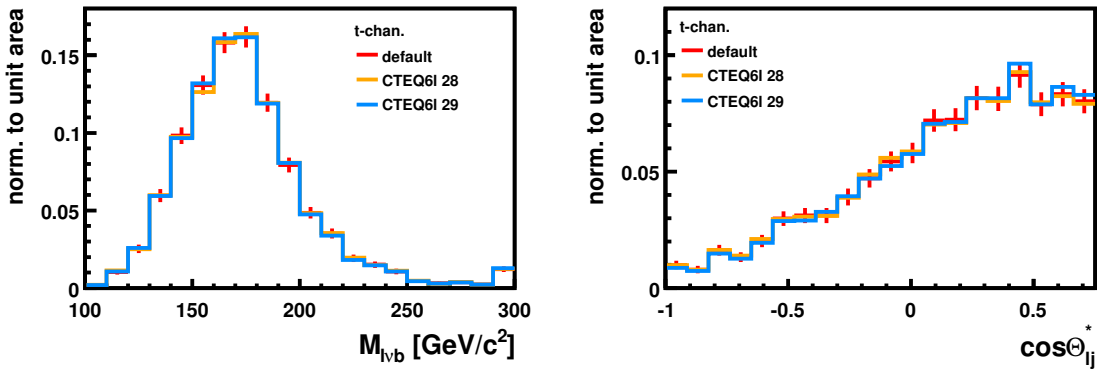

(a) (b)

Figure 23: Reconstructed top quark mass (a) and $\cos\theta^*_{lj}$ (b) for signal events, with PDF sets n.28 and 29 of the CTEQ61 collection.

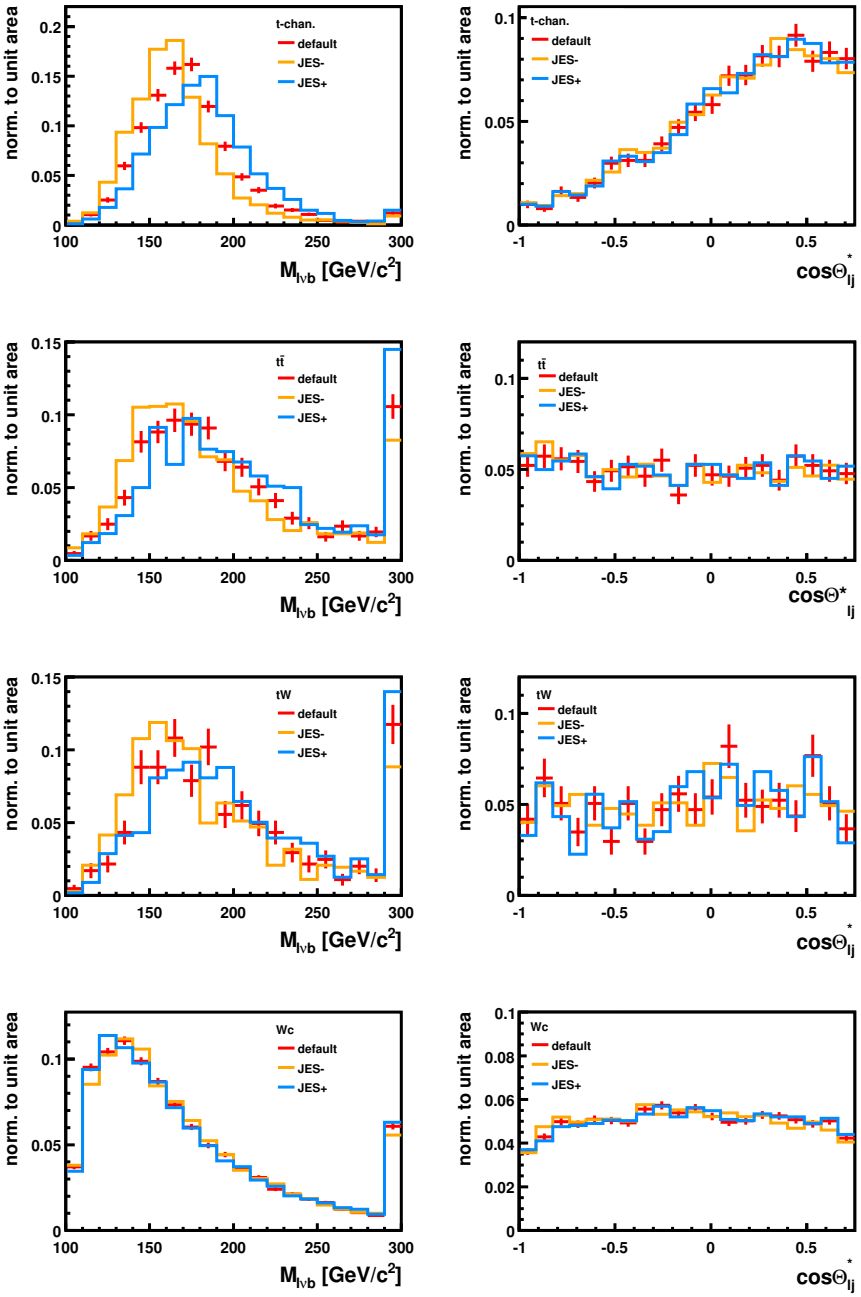

Figure 24: Reconstructed top quark mass (left) and $\cos\theta^*_{lj}$ (right), with rescaled JES, for signal (first row), $t\bar{t}$ (second row), tW (third row) and Wc (fourth row).

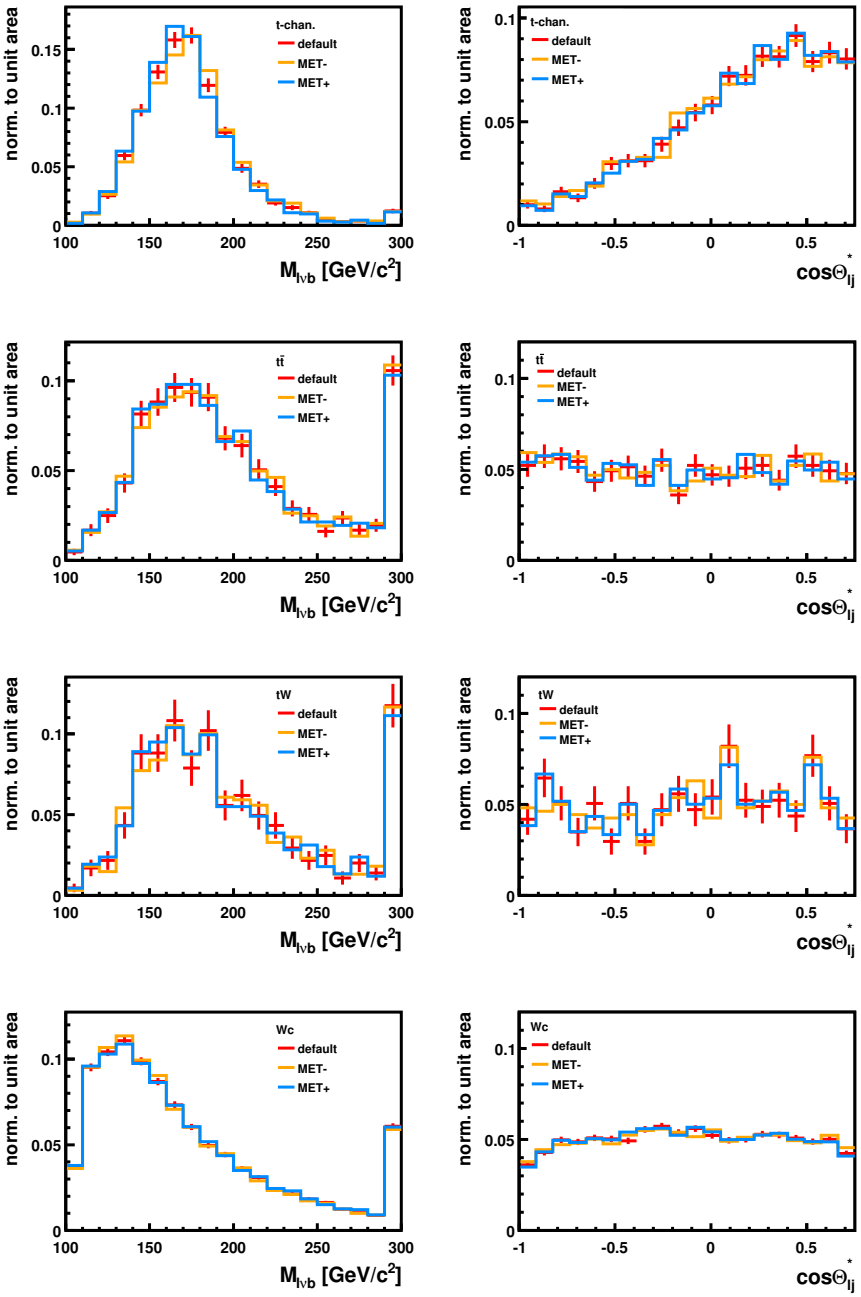

Figure 25: Reconstructed top quark mass (left) and $\cos\theta^*_{lj}$ (right), with rescaled uncorrected $\not{E}_{\mathrm{T}}$, for signal (first row), $t\bar{t}$ (second row), tW (third row) and Wc (fourth row).

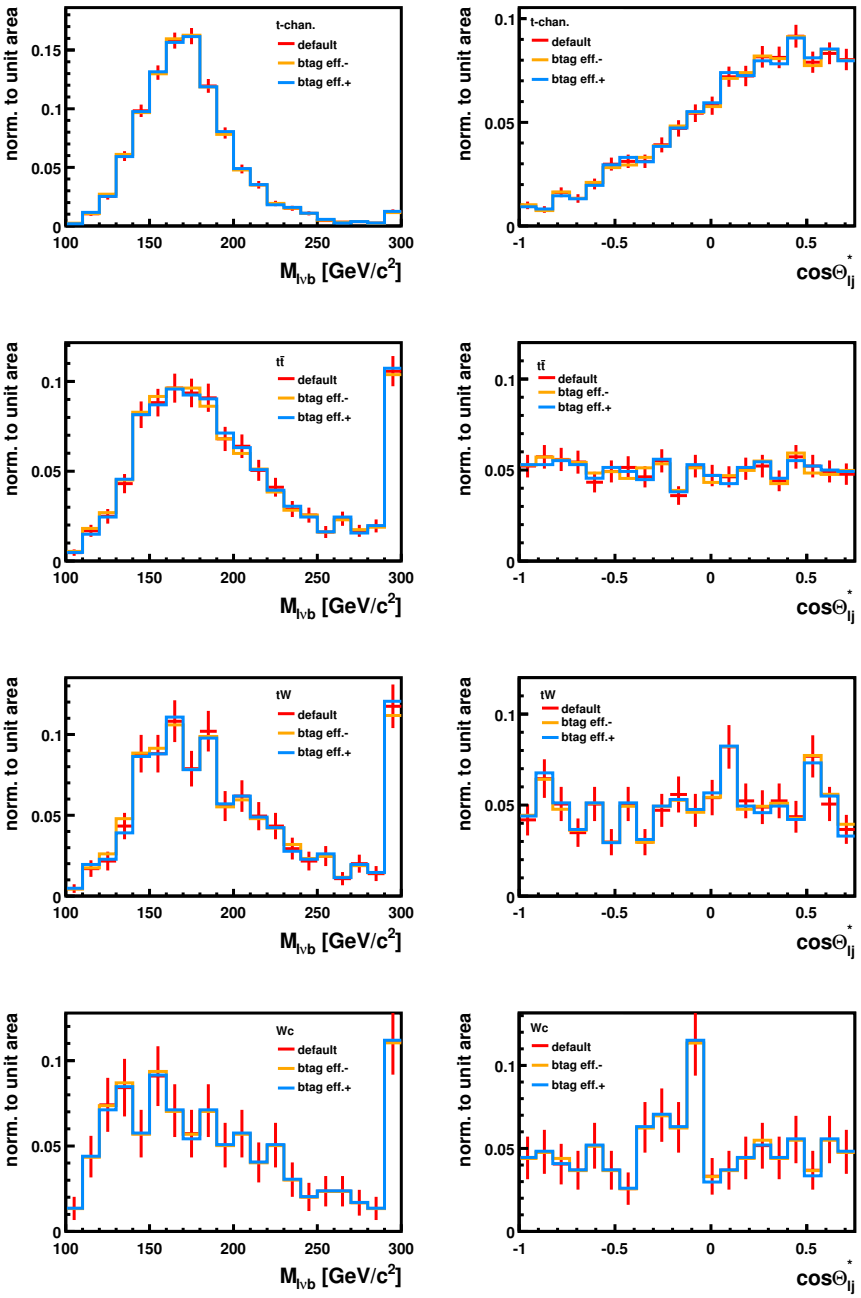

Figure 26: Reconstructed top quark mass (left) and $\cos\theta^*_{lj}$ (right), with variated b-tagging efficiency, for signal (first row), $t\bar{t}$ (second row), tW (third row) and Wc (fourth row).

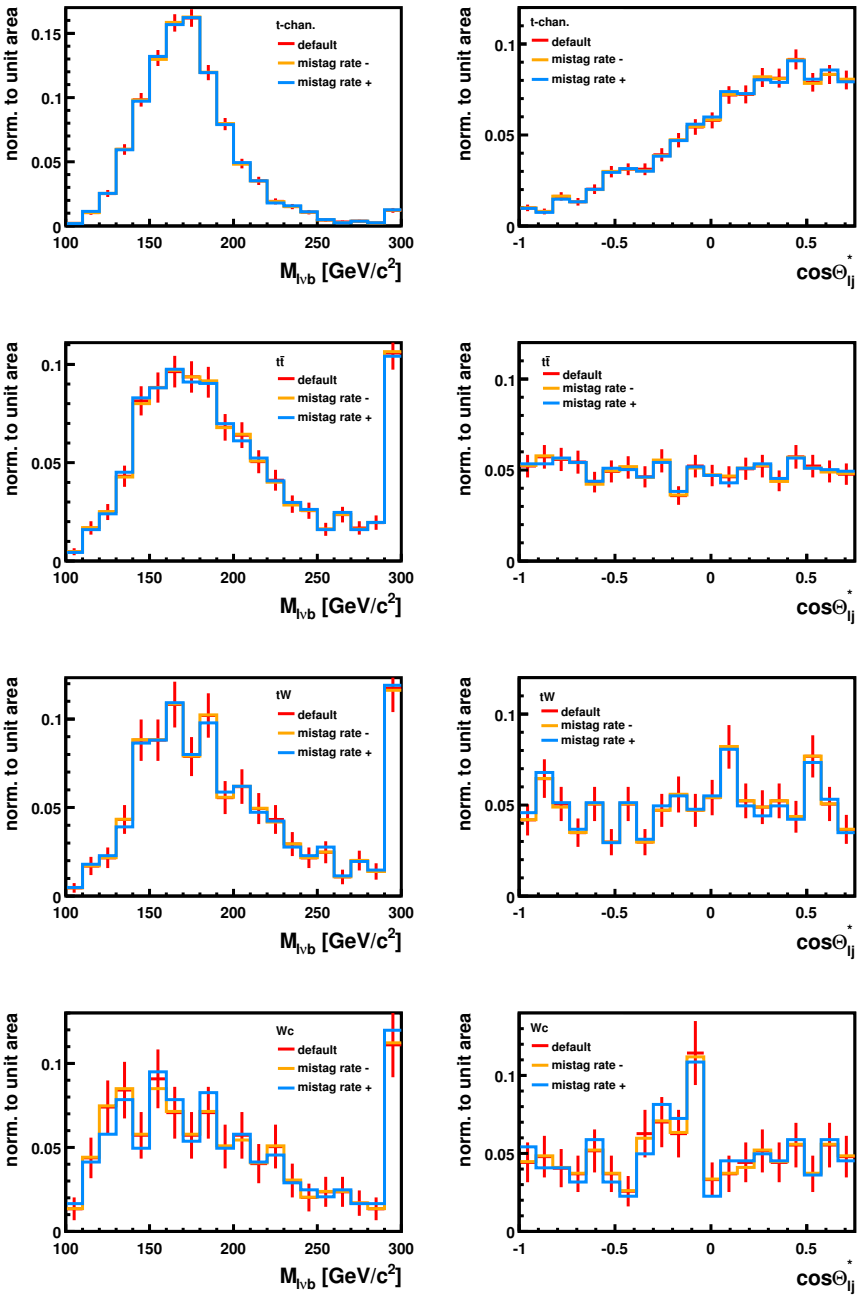

Figure 27: Reconstructed top quark mass (left) and $\cos\theta^*_{lj}$ (right), with variated mistagging efficiency, for signal (first row), $t\bar{t}$ (second row), tW (third row) and Wc (fourth row).

Variated parameter	Dataset name
Generator (PYTHIA+Tauola)	/TauolaTTbar/Summer08_IDEAL_V9_AODSIM_v1/AODSIM
Detector simulation (FastSim)	/pedros-TauolaTT_nominalISRFSR_v1-b8a0743b92124a143352d416e0ab9f0d/USER
More ISR/FSR (FastSim)	/pedros-TauolaTT_largeISRFSR_v1-cf21f75fded96c34a643b446d0371ed5/USER
Less ISR/FSR (FastSim)	/pedros-TauolaTT_smallISRFSR_v1-ac11a739a480b3ff057562a4afebcd8d/USER

Table 13: Samples used for systematics related to $t\bar{t}$ modeling.

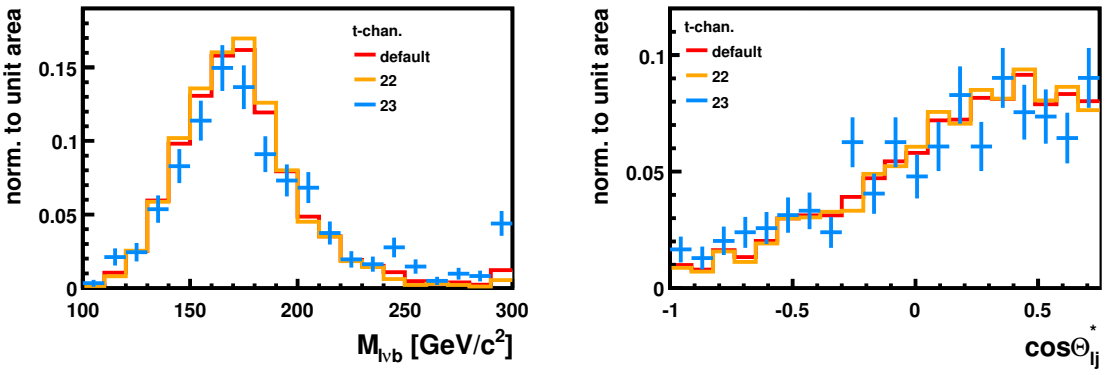

(a) (b)

Figure 28: Reconstructed top quark mass (a) and $\cos\theta^*_{lj}$ (b), for signal events produced by the matching procedure (*default*) and by the $2 \to 2$ and $2 \to 3$ processes only.

see Table 13.

The relevant settings variated in PYTHIA between the three samples are:

- for the sample with reduced ISR/FSR, the power shower was switched off (`MSTP(68)`$= 1$)
- for the sample with larger ISR/FSR, the parameter `PARP(64)`, related to Q^2_{max}, was set to one (reference: 0.2), and the following parameters related to Λ_{QCD} were modified (with `MSTP(3)` $= 1$, meaning that their values are not overridden): `PARP(61)` $= 0.35$ (reference: 0.25), `PARP(72)` $= 0.35$ (reference: 0.25), and `PARJ(81)` $= 0.35$ (reference: 0.25).

The number of jets in these samples is compared in Fig. 29. The impact of the variation on the $M_{l\nu b}$ and $\cos\theta^*_{lj}$ shapes is shown in Fig. 30. The corresponding variation in event yield is -6.3% (ISR/FSR up) and $+14.5\%$ (ISR/FSR down).

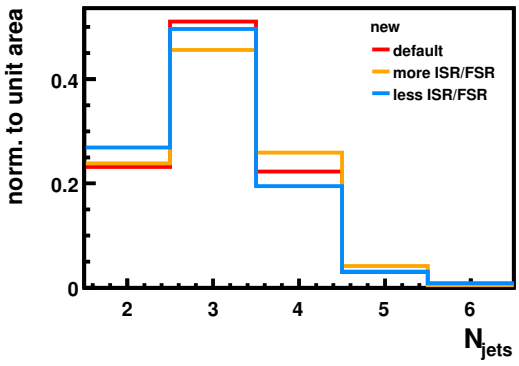

Figure 29: Jet multiplicities for $t\bar{t}$ PYTHIA+FastSim samples with variated ISR/FSR settings. The distributions are extracted from the pretag sample since the final selection yields too few events.

As a further robustness test, in Fig. 31 we compare the same shapes between the MadGraph sample used so far and a PYTHIA sample interfaced with the Tauola package [55]. No significant difference is noticed, within the statistical uncertainty. The event yield, instead, is lower by 10% with respect to the MadGraph sample.

7.6 Unflatness of the background shape for $\cos\theta^*_{lj}$

We consider the deviations from flatness of $\cos\theta^*_{lj}$ for the main background components, separately (see Fig. 17).The description of the template extraction procedure can be found in Sec. 6.2.

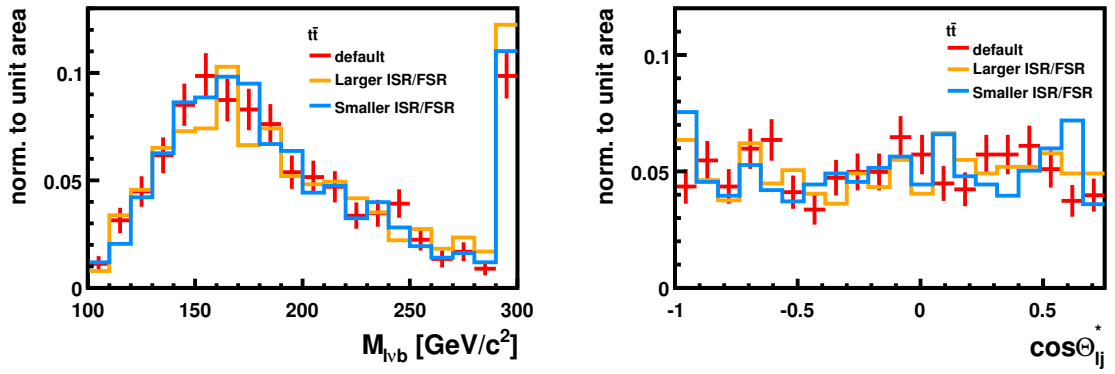

(a) (b)

Figure 30: Reconstructed top quark mass (a) and $\cos\theta^*_{lj}$ (b), for $t\bar{t}$ PYTHIA+FastSim samples with variated ISR/FSR settings. The distributions are extracted from the pretag sample since the final selection yields too few events.

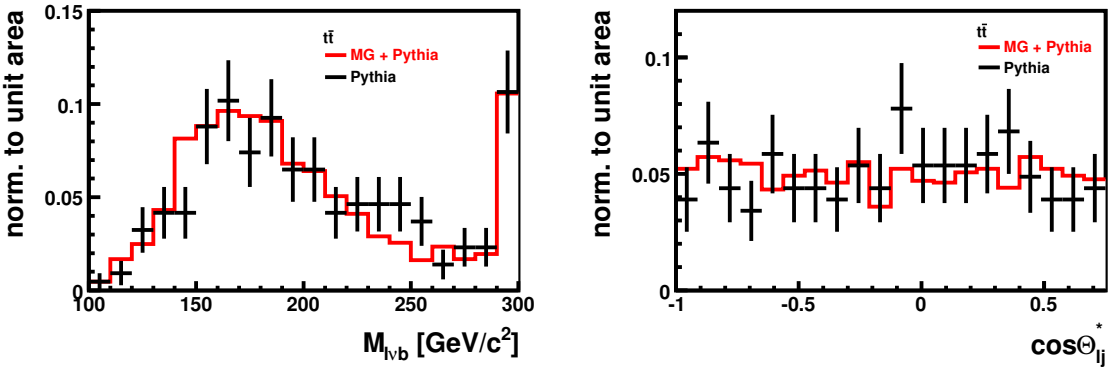

(a) (b)

Figure 31: Reconstructed top quark mass (a) and $\cos\theta^*_{lj}$ (b), for $t\bar{t}$ events generated with MadGraph and with PYTHIA+Tauola.

Process	PDF	JES	$\not\!\!E_{\rm T}$	ϵ_{btag}	ϵ_{mistag}
single top, t channel	$^{+5.8\%}_{-4.5\%}$	$^{-0.2\%}_{-1.6\%}$	$^{+4.7\%}_{-6.4\%}$	$^{-6.8\%}_{+7.2\%}$	$^{+0.1\%}_{-0.4\%}$
single top, s channel	-	$^{+3.0\%}_{-3.0\%}$	$^{+1.5\%}_{0.0\%}$	$^{+9.4\%}_{-11.1\%}$	≈ 0
single top, tW	$^{+3.4\%}_{-3.9\%}$	$^{-13.9\%}_{+11.9\%}$	$^{+4.2\%}_{-5.9\%}$	$^{-5.1\%}_{+6.5\%}$	$^{+0.5\%}_{-0.3\%}$
$t\bar{t}$	$^{+2.9\%}_{-3.2\%}$	$^{-23.4\%}_{+24.8\%}$	$^{+3.8\%}_{-5.3\%}$	$^{-0.9\%}_{-0.1\%}$	$^{+0.1\%}_{-0.3\%}$
dibosons (WW,WZ,ZZ)	-	$^{+4.1\%}_{+4.1\%}$	$^{+10.8\%}_{-8.1\%}$	$^{+1.3\%}_{+1.7\%}$	$^{-13\%}_{+11\%}$
$W+X$	-	$^{+14.8\%}_{-9.9\%}$	$^{+10.1\%}_{-8.4\%}$	$^{+0.3\%}_{-1.1\%}$	$^{-12.3\%}_{+8.8\%}$
Total background		$^{-11.0\%}_{+15.5\%}$	$^{+7.4\%}_{-7.6\%}$	$^{-1.1\%}_{+0.3\%}$	$^{-3.4\%}_{+1.9\%}$

Table 14: Systematic uncertainties on the event yields for the signal and the main backgrounds.

We expect this to be an overestimation of the actual shape uncertainty, since *a priori* we don't expect any deviation from flatness, far from the $\cos\theta^*_{lj} \approx 1$ region where isolation and near-jet veto bias the distribution, and the small observed deviations can be accounted as statistical fluctuations.

7.7 Luminosity uncertainty

A 10% uncertainty is expected to be achieved on the luminosity from dedicated measurements [56].

7.8 Impact of the overall background size

In the case of the fit to $\cos\theta^*_{lj}$ with the assumption of a flat background, we consider a $\pm$ 50% variation of the overall background size. No bias is introduced in the cross section determination, as expected, and the statistical uncertainty becomes 40.8% and 27.8 % for upward and downward variations respectively. With 50% probability, in the two scenarios, we get 2.2σ and 3.2σ excesses over the H_0 hypothesis, respectively.

7.9 Effect on signal extraction

The effects of the PDF variation and of the systematic uncertainties of instrumental origin (JES, $\not\!\!E_{\rm T}$, b tagging) on the event yields are summarized in Table 14 for the signal and the main backgrounds. For other samples the limited number of surviving MC events makes difficult to draw quantitative conclusions.

The acceptance and shape uncertainties are incorporated in the pseudo experiments of the ensemble tests described in the section 6. Systematic rate uncertainties are taken into account by drawing the number of events N_j of a process j according to a Poisson (unconstrained processes) or a Gaussian (constrained processes) with a modified mean $\hat{\nu}'_j$ instead of $\hat{\nu}_j$:

$$\hat{\nu}'_j = \hat{\nu}_j \cdot \prod_{i=1}^{S} (1 + |\delta_i| \cdot (\epsilon_{ji+} H(\delta_i) + \epsilon_{ji-} H(-\delta_i))). \tag{20}$$

Here, S is the number of systematic rate uncertainties, i is the index of the systematic rate uncertainties, δ_i indicates the strength of the systematic uncertainty i, ϵ_{ij} represents the relative rate uncertainties for process j and $H(x)$ denotes the Heaviside step function. The δ_i are drawn from Gaussian distributions centered at zero with unit standard deviation.

After that, N_j random numbers are drawn from the systematically shifted template distributions α'_{jk} of the physical process j:

$$\alpha'_{jk} = \alpha_{jk} \cdot \sum_{l=1}^{S'} (1 + |\delta_l| \cdot (\kappa^+_{jlk} H(\delta_l) + \kappa^-_{jlk} H(-\delta_l))). \tag{21}$$

Here, S' is the number of systematic shape uncertainties considered, l is the index of the systematic shape uncertainties, δ_l indicates the strength of the systematic uncertainty l, and $\kappa^{\pm}_{jlk}$ represents the relative shape uncertainies for process j. If a systematic effect causes both, rate and shape uncertainties, δ_i and δ_l have the same value. The $\kappa^{\pm}_{jlk}$ are derived from normalized, systematic shifted histograms (α^+_{jlk} and α^-_{jlk}) which take different scenarios of a systematic uncertainty into account. They are calculated via:

$$\kappa^{\pm}_{jlk} = \frac{\alpha^{\pm}_{jlk} - \alpha_{jk}}{\alpha_{jk}} \tag{22}$$

	$\cos\theta^*_{lj}$			$M_{l\nu b}$		
Source of uncertainty	rate	shape	rate + shape	rate	shape	rate + shape
PDF	$^{+5.8\%}_{-4.5\%}$	$^{-0.5\%}_{-0.1\%}$	$^{5.5\%}_{-4.7\%}$	$^{5.0\%}_{-5.2\%}$	$^{-0.1\%}_{0.1\%}$	$^{4.9\%}_{-5.0\%}$
JES	$^{-0.2\%}_{-1.1\%}$	$^{-1.0\%}_{-3.5\%}$	$^{-1.3\%}_{-5.5\%}$	$^{-11.3\%}_{11.1\%}$	$^{-32.1\%}_{8.6\%}$	$^{-40.9\%}_{21.5\%}$
MET	$^{+4.8\%}_{-6.2\%}$	$^{1.7\%}_{-3.3\%}$	$^{6.2\%}_{-9.9\%}$	$^{7.0\%}_{-9.2\%}$	$^{2.0\%}_{-5.4\%}$	$^{8.9\%}_{-14.5\%}$
b tagging	$^{-6.5\%}_{7.3\%}$	-	-	$^{-7.4\%}_{6.9\%}$	-	-
mistagging	$^{\approx 0\%}_{-0.4\%}$	-	-	$^{-0.3\%}_{-0.4\%}$	-	-
Signal modeling ($^{2\to 2}_{2\to 3}$)	-	$^{+4.8\%}_{-8.5\%}$	-	-	$^{4.0\%}_{-12.4\%}$	-
$t\bar{t}$ modeling - Pythia	-	-	-	-4.7%	-8.3%	-12.5%
$t\bar{t}$ ISR/FSR	-	-	-	$^{-3.2\%}_{7.8\%}$	$^{-8.9\%}_{-12.1\%}$	$^{-11.4\%}_{-6.4\%}$
$t\bar{t} + tW$ shape	-	-1.8%	-	-	-	-
$W/Z + X$ shape	-	$+11.6\%$	-	-	-	-
QCD shape	-	-14.7%	-	-	-	-

Table 15: Impact of the systematic uncertainties on the β_{signal} values extracted from the fit on $\cos\theta^*_{lj}$ amd $M_{l\nu b}$. respectively. The strength of the systematic effects is fixed to the 1σ deviation, thus the data distributions in the pseudo experiments are obtained from equations 23, 24.

Source of uncertainty	Rate only	Shape only	Rate and shape
Statistical	-	-	3.8σ
Signal modeling	-	3.8σ	-
$t\bar{t}$ modeling	-	3.6σ	-
PDF	3.6σ	3.6σ	3.6σ
JES	3.4σ	3.6σ	3.5σ
$\not{E}_{\mathrm{T}}$ scale	3.6σ	3.8σ	3.5σ
b tagging	3.6σ	-	-
mistagging	3.6σ	-	-
Total systematic	3.1σ	2.7σ	2.7σ

Table 16: Impact of the systematic uncertainties on the expected sensitivities from the fit to the reconstructed top-quark mass $M_{l\nu b}$.

and fulfill $\sum_{k=1}^{B} \alpha_{jk} \cdot \kappa^{\pm}_{jlk} = 0$. The δ_l are drawn from Gaussian distributions which are centered at zero with standard deviation one.

The further statistical treatment is the same as without systematic uncertainties (see section 6). For each pseudo experiment and for both ensemble tests (H_0, H_1) two binned likelihood fits are performed. One with β_{signal} as free parameter and a second fit, where $\beta_{signal} = 0$ is fixed. The Q-value distributions for both ensemble tests are determined, see Fig. 32, and the expected p-value as well as the sensitivity of the analysis are determined.

In addition, the impact of the different systematic effects were studied under the assumption of a fixed strength of 1σ for each source of uncertainty i. For these cases, equations 20 and 21 can be simplified to:

$$\hat{\nu}'^{\pm}_{ji} = \hat{\nu}^{\pm}_{ji} \cdot (1 + (\epsilon^{\pm}_{ji})), \tag{23}$$

$$\alpha'^{\pm}_{jk} = \alpha^{\pm}_{jk} \cdot (1 + \kappa^{\pm}_{jlk}). \tag{24}$$

Deviations in the negative and positive direction are treated in separate ensemble tests. The uncertainties on the fitted cross-section value obtained from 10,000 pseudo experiments based on this conservative estimation are summarized in Table 15 for all the considered sources of systematic effects and both observables. We symmetrize these uncertainties by taking the absolute value of the maximum deviation, and we obtain a total systematic uncertainty of 14% in the $\cos\theta^*_{lj}$ case.

The effect of the individual sources of uncertainty on the expected sensitivity is shown in Tables 16 and 17 for $M_{l\nu b}$ and $\cos\theta^*_{lj}$, respectively.

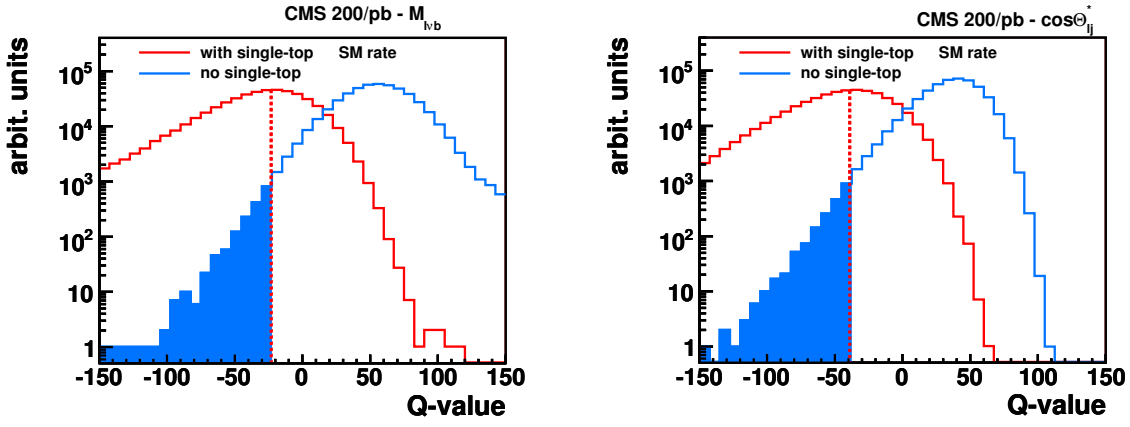

(a) (b)

Figure 32: Q-value distributions for $M_{l\nu b}$ in scenario S_1 (a) and $\cos\theta^*_{lj}$ in scenario S_{flat} (b), with 200 pb^{-1}.

Source of uncertainty	Expected sensitivity
Statistical	2.8σ
PDF	2.7σ
JES	2.7σ
MET scale	2.7σ
b tagging	2.7σ
mistagging	2.7σ
Statistical + systematic	2.7σ
$t\bar{t} + tW$ shape	2.7σ
$W/Z + X$ shape	2.7σ
QCD shape	2.6σ
Signal modeling	2.9σ
$+50\%$ background	2.2σ
-50% background	3.2σ

Table 17: Impact of the systematic uncertainties on the expected sensitivity of the fit to $\cos\theta^*_{lj}$.

8 Conclusions and Outlook

The central result of the analysis presented here is that it is realistic to provide the first evidence of single top in a pp collider with ≈ 200 pb^{-1} of data at 10 TeV.

Two complementary discriminating variables would provide the needed separation of signal from background, after a selection optimized for the dominant t channel, based on two striking features of the signal:

- the presence of only one top in the event, recognizable from the relatively narrow peak in the invariant mass distribution $M_{l\nu b}$ (while it is broadened by combinatorics in $t\bar{t}$ events);
- the $\approx 100\%$ polarization of the top quark, which is entirely propagated to the decay muon, yields a very typical muon angular distribution $\cos\theta^*_{lj}$.

Fitting the $\cos\theta^*_{lj}$ distribution has the following advantages:

- the shape of the distribution seems to be very little affected by all the modeling and detector systematics considered so far;
- all the backgrounds have an almost flat distribution, permitting to neglect the distinctions and to fit an overall background pedestal, assumed to be perfectly flat in the fit range.

This procedure yields a statistical cross section uncertainty of 35%, which moves to 40.8% and 27.8 % when the overal background is rescaled by $+50\%$ and -50% respectively. Systematic uncertainties sum up to 14% (not including the luminosity uncertainty, foreseen to be 10%).

The $M_{l\nu b}$ fit has a better discriminating power, in principle, yielding a 26% statistical error on the cross section when using a 20% Gaussian constraint on $t\bar{t}$, and the ability to simultaneously discriminate between signal, $t\bar{t}$, and $W/Z + X$ processes even with no constraints (31% statistical error in this case). On the other hand, this variable is more affected by systematic effects concerning the number and kinematics of the visible jets in the event. Under the assumptions of the present study, the Jet Energy Scale uncertainty dominates the cross section uncertainty from the $M_{l\nu b}$ fit. Before trusting its results completely, with real data, a reasonable control of the detector and of the gluon-radiation modeling of the main backgrounds will have to be demonstrated.

Special attention has been paid to the data-driven estimation of QCD events (although unimportant when an homogeneous overall background is assumed, as in the $\cos\theta^*_{lj}$ fit in the standard fitting scenario). The method chosen is a template fit in the M_T variable. It yields a correct prediction within the statistical uncertainty of our MC sample.

Several other features of the signal can provide confirmation to the presence of signal, like the pseudorapidity distribution of the untagged jet (see Fig. 33), but these would be more affected by theoretical uncertainties of presently unknown size, thus have been discarded for the present study. Nevertheless, it will be interesting to check it with data: it would provide an additional confirmation that the selected sample is actually enriched in single-top events, and it would eventually prove precious for the Monte Carlo tuning and the theory validation.

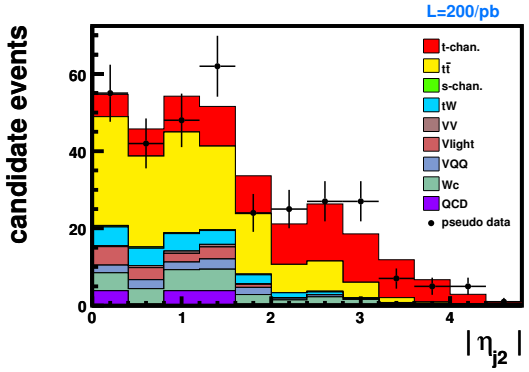

Figure 33: Pseudo-rapidity distribution of the second jet after full selection, normalized to 200 pb^{-1}.

8.1 Future analysis developments

While the focus of this note has been explicitly set on updating and improving the previous results at 14 TeV [9], the highest priority is now to prepare the analyses to be run with the very first LHC data.

Nevertheless, we believe that the present selection, although already satisfactory from the point of view of the statistical significance, could be further improved if more time were to be devoted to the task, by intervening in the following area:

- τ-jet veto: in the current analysis, τ-id is not used at all, and a τ jet is usually identified as a normal jet from quark or gluon;
- veto of electromagnetic objects in HF: the HF calorimeter acts simultaneously as an electromagnetic and hadronic calorimeter and, although this feature has not been exploited in the present analysis, this can further reduce the $t\bar{t} \rightarrow 2l$ background when the second lepton is an electron and falls in the HF acceptance, giving a fake "forward jet";
- use of the Particle Flow technique: this is expected to give more reliable $\not\!\!E_{\rm T}$ and jet-multiplicity measurements, with potential benefits to the analysis as shown by a preliminary investigation [57].

None of the items of this list are crucial for the analysis, and realistically they would only provide a marginal improvement in the results. Nonetheless, it is useful to keep in mind that additional handles for selection are

potentially available.

A much more important addition would be the electronic channel, which would require some extra care from the point of view of the QCD contamination and its control from data. Ideally, with an electronic selection as efficient and as pure as the muonic one, the statistical error on the cross section would be expected to shrink by a factor $\approx \sqrt{2}$, since this analysis is statistics-dominated for the considered amount of data.

Although the template-fit method has been demonstrated to depend very little on the prior knowledge of the background contamination, in particular for the $\cos\theta^*_{lj}$ variable which has a very similar shape for all the backgrounds, one can argue that an independent estimation of the main backgrounds would provide an important cross-check. Furthermore, on the long term one would like to use $\cos\theta^*_{lj}$ as a tool to investigate the presence of non-SM contributions to single-top production: processes where the virtual W is replaced by a different particle (as in many theories where FCNC couplings enhance the cross section [8]) would in general be flat in this variable, therefore an independent background subtraction would permit to search for new physics under the form of a pedestal in the $\cos\theta^*_{lj}$ distribution.

Possible data-driven methods to estimate the main backgrounds:

- $t\bar{t} \rightarrow 1\mu + jets$: in the context of the $WW \rightarrow 2l$ analysis a method has been developed to estimate this contamination from data, by counting the number of muons inside jets [58];
- $W + X$: the selection described in Sec. 3 apart from the central second-jet veto, applied to the other jet multiplicities, yields the background contaminations visible in Fig. 34. It can be seen that, despite the b tagging, the 1-jet bin is still dominated by $W + X$ events. Since the normalization of this process has a large uncertainty, it is envisageable to use this bin to constrain the $W + X$ contamination in the 2-jets bin.

A complementary signal-extraction method makes use of the charge asymmetry of the single-top production in t channel. This has been preliminarily explored in a previous study at 14 TeV [9], and proved to be very robust against systematic errors, with the exception of PDF, and against background contamination, with the exception of $W + X$ (which is charge-asymmetric too). The main limitation comes from an increased statistical uncertainty, and in a 200 pb^{-1} scenario this method will not be competitive yet [59].

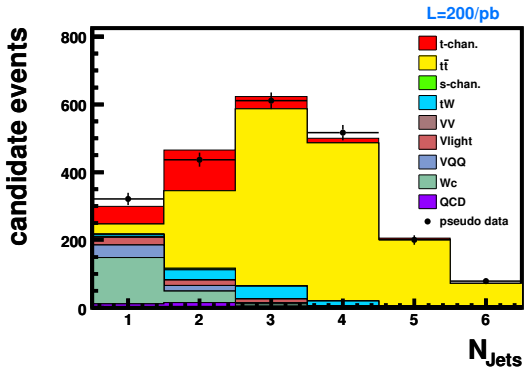

Figure 34: Jet multiplicity after complete selection, apart from b veto.

Acknowledgements

We wish to thank Claudio Campagnari, Tim Christiansen, Slava Krutelyov, Jorgen D'Hondt, Roberto Tenchini, Frank-Peter Schilling, Fabio Maltoni and the MadGraph team, Roberto Chierici, Jérémy Andrea, Robert Harris, Philipp Schieferdecker, Christophe Saout, Silvano Tosi, Maxim Perfilov, Salvatore Rappoccio, Keith Hamilton, Cecilia Gerber and Nadia Pastrone.

References

[1] B.W. Harris et al., "The fully differential single-top-quark cross section in next-to-leading order QCD", Phys.Rev. D66 (2002) 054024, arXiv:hep-ph/0207055

[2] N. Kidonakis, "Higher-order soft gluon corrections in single top quark production at the LHC", Phys.Rev. D75 (2007) 071501, arXiv:hep-ph/0701080

[3] J. Campbell, F. Tramontano, "Next-to-leading order corrections to Wt production and decay", Nucl.Phys. B726 (2005) 109-130, arXiv:hep-ph/0506289

[4] The D0 Collaboration, "Observation of single top quark production", arXiv:0903.0850[hep-ex]

[5] The CDF Collaboration, "First Observation of Electroweak Single Top Quark Production", arXiv:0903.0885v2[hep-ex]

[6] J. Alwall et al., "Is $|V_{tb}| \approx 1$?", Eur Phys.J., C49, 791-801 (2007), arXiv:hep-ph/0607115v2

[7] B. Holdom et al., "Four statements about the fourth generation", arXiv:0904.4698[hep-ph]

[8] T.M.P. Tait, C.-P. Yuan, "Single Top Production as a Window to Physics Beyond the Standard Model", Phys.Rev.D63:014018 (2001), arXiv:hep-ph/0007298

[9] A. Giammanco et al., "Towards a measurement of single-top cross section in the t channel, with the first inverse femtobarn of CMS data at 14 TeV", CMS Analysis Note 2009/026

[10] Proceedings of the 2009 Chamonix workshop on LHC performance, CERN-ATS-2009-001
https://espace.cern.ch/acc-tec-sector/Chamonix/Chamx2009/html/session.htm

[11] The CMS Collaboration, " First CMS Results from CRAFT", CMS DP-2009/002
http://cmsdoc.cern.ch/cms/performance/tracker/conferences/CRAFT_TK_Approved.ppt

[12] F. Maltoni and T. Stelzer, "MadEvent: Automatic event generation with MadGraph", JHEP **0302**, 027 (2003), arXiv:hep-ph/0208156

[13] E. Boos et al., "Method for simulating electroweak top-quark production events in the NLO approximation: SingleTop event generator", Phys.Atom.Nucl. 69, 8 (2006) 1317

[14] S. Frixione and B. R. Webber, "Matching NLO QCD computations and parton shower simulations", JHEP **06**, 029 (2002), arXiv:hep-ph/0204244

[15] L. Dudko et al., "Comparison of the different Monte-Carlo models for the t-channel single top quark production", CMS Analysis Note 2009/024

[16] Calculated by M. Perfilov (private communication) with MCFM [17]

[17] http://mcfm.fnal.gov/

[18] J. Pumplin, D. R. Stump, J. Huston, H. L. Lai, P. Nadolsky and W. K. Tung, "New Generation of Parton Distributions with Uncertainties from Global QCD Analysis", JHEP 0207 (2002) 012 [arXiv:hep-ph/0201195]

[19] C. Amsler et al., "Review of Particle Physics", Physics Letters B 667 (2008) 1

[20] https://twiki.cern.ch/twiki/bin/view/CMS/SWGuideFlavorHistory

[21] J. Alwall et al., "Comparative study of various algorithms for the merging of parton showers and matrix elements in hadronic collisions", Eur.Phys.J.C53 (2008) 473-500

[22] J. Allison et al., "Geant4 developments and applications", IEEE Transactions on Nuclear Science 53 No. 1 (2006) 270-278

[23] http://lhc-commissioning.web.cern.ch/lhc-commissioning/luminosity/09-10-lumi-estimate.htm

[24] J. Campbell, R.K. Ellis, F. Tramontano, "Single top production and decay at next-to-leading order", Phys. Rev. D70 (2004), 094012;
rescaled to 10 TeV by S. Tosi (private communication) according to the ratio of the leading-order cross sections calculated with MadGraph [12].

[25] J. Campbell, F. Tramontano, "Next-to-leading order corrections to Wt production and decay", Nucl. Phys. B726 (2005), 109;
rescaled to 10 TeV by S. Tosi (private communication) according to the ratio of the leading-order cross sections calculated with MadGraph [12].

[26] M. Cacciari, S. Frixione, M.L. Mangano, P. Nason, G. Ridolfi, "Updated predictions for the total cross sections for top and of heavier quark pairs at the Tevatron and at the LHC", JHEP 0809 (2008), 127; arXiv:0804.2800[hep-ph]

[27] Calculated by S. Tosi with MCFM, v5.3 [17]

[28] `https://twiki.cern.ch/twiki/bin/view/CMS/SWGuidePAT`

[29] `https://twiki.cern.ch/twiki/bin/view/CMS/TSG_18_II_09_1E31`

[30] M. Mulders et al., "Muon identification in CMS", CMS Analysis Note 2008/098

[31] The CMS Collaboration, "CMS Physics TDR: Volume I (PTDR1), Detector Performace and Software", CERN-LHCC-2006-001; Chapter 10, "Electrons and Photons"

[32] `https://twiki.cern.ch/twiki/bin/view/CMS/SWGuideElectronID`

[33] F. Bostock, talk given in `http://indico.cern.ch/conferenceDisplay.py?confId=32732`

[34] The UA1 Collaboration, "Observation of jets in high transverse energy events at the CERN proton antiproton collider", Phys. Lett. B 123, 115 (1983)

[35] The CMS Collaboration, "Plans for Jet Energy Corrections at CMS", CMS PAS JME-07-002

[36] `https://twiki.cern.ch/twiki/bin/view/CMS/SWGuideBTagging`

[37] M. Narain et al., "Performance Measurement of b tagging Algorithms Using Data containing Muons within Jets", CMS Analysis Note 2007/046
The CMS Collaboration, CMS PAS BTV-07-001

[38] J. Andrea et al., "Evaluation of $udsg$ Mistag Rate of b-tag Jets using Negative Tags", CMS Analysis Note 2007/048
The CMS Collaboration, CMS PAS BTV-07-002

[39] `https://twiki.cern.ch/twiki/bin/view/CMS/MuonIsolationSelections2XY`

[40] S. Esen et al., "Missing E_T Performance in CMS", CMS Analysis Note 2007/041

[41] D. Konstantinov and A. Giammanco, talk given in
`http://indico.cern.ch/conferenceDisplay.py?confId=44329`

[42] J.E. Gaiser, Appendix F of "Charmonium spectroscopy from radiative decays of the J/ψ and ψ'", PhD thesis, SLAC-R-255 (1982)

[43] J. Kiefer et al., "Observability of Top Quark Pair Production in the Semileptonic Muon Channel with the first 10 pb^{-1} of CMS Data", CMS Analysis Note 2008/014.
The CMS Collaboration, CMS PAS TOP-08-005

[44] J. Kiefer, talk given in
`http://indico.cern.ch/contributionDisplay.py?contribId=2&confId=51557`

[45] P. Biallass et al., "Parton Distribution uncertainty determination with CMSSW", CMS Analysis Note 2009/048

[46] G. Majumder et al., "Muon Differential Cross Sections and Charge Asymmetry in Inclusive $pp \to W(\mu\nu) + X$ Production at $\sqrt{s}$=10 TeV", CMS Analysis Note 2009/054

[47] G. Mahlon and S. Parke, "Improved Spin Basis for Angular Correlation Studies in Single Top Quark Production at the Tevatron", Phys.Rev. D55, 7249 (1997), arXiv:hep-ph/9611367

[48] G. Mahlon and S. Parke, "Single Top Quark Production at the LHC: Understanding Spin", Phys.Lett. B476 (2000), arXiv:hep-ph/9912458

[49] P. Motylinski, "Angular correlations in t-channel single top production at the LHC", arXiv:0905.4754[hep-ph]

[50] M. Renz, "B-Jet and C-Jet identification with neural networks as well as combination of multivariate analyses for the search for single top-quark production", IEKP-KA/2008-17, http://www-ekp.physik.uni-karlsruhe.de/pub/web/thesis/iekp-ka2008-17.pdf

[51] F. James and M. Roos, "A system for function minimization and analysis of the parameter errors and correlations", Comp.Phys.Comm. 10 (1975) 343-367

[52] V. Abramov et al., "Selection of Single Top Events with the CMS Detector at LHC", CMS NOTE 2006/084

[53] https://twiki.cern.ch/twiki/bin/view/CMS/SWGuideFastSimulation

[54] P. Bartalini, R. Chierici and A. De Roeck, "Guidelines for the estimation of theoretical uncertainties at the LHC", CMS NOTE 2005/013

[55] R. Decker et al., "The tau decay library TAUOLA: version 2.4", Comp.Phys.Comm.76-3 (1993) 361-380

[56] H. Jung et al., "Proceedings of the workshop: HERA and the LHC workshop series on the implications of HERA for LHC physics", arXiv:0903.3861[hep-ph]

[57] A. Giammanco, talk given in http://indico.cern.ch/conferenceOtherViews.py?view=cdsagenda&confId=35611

[58] D. Kovalskyi, talk given in http://indico.cern.ch/conferenceDisplay.py?confId=40788

[59] A. Giammanco and M. Mohammadi Najafabadi, talk given in http://indico.cern.ch/conferenceDisplay.py?confId=53263